

# An *XMM-Newton* view of M101 - II. Global X-ray source properties

L.P. Jenkins<sup>1</sup>\*, T.P. Roberts<sup>1</sup>, R.S. Warwick<sup>1</sup>, R.E. Kilgard<sup>1,2</sup>, M.J. Ward<sup>1</sup>

<sup>1</sup> X-ray & Observational Astronomy Group, Dept. of Physics & Astronomy, University of Leicester, University Road, Leicester LE1 7RH, U.K.

<sup>2</sup> Harvard-Smithsonian Center for Astrophysics, 60 Garden Street, Cambridge, MA 02138, USA.

Accepted .....; Received .....; in original form .....

## ABSTRACT

We present the global X-ray properties of the point source population in the grand-design spiral galaxy M101, as seen with *XMM-Newton*. 108 X-ray sources are detected within the D<sub>25</sub> ellipse of M101, of which  $\sim 24$  are estimated to be background sources. Multiwavelength cross-correlations show that 20 sources are coincident with HII regions and/or supernova remnants (SNRs), 7 have identified/candidate background galaxy counterparts, 6 are coincident with foreground stars and one has a radio counterpart. While the spectral and timing properties of the brightest sources were presented in Jenkins et al. (2004), here we apply an X-ray colour classification scheme to split the entire source population into different types, i.e. X-ray binaries (XRBs), SNRs, absorbed sources, background sources and supersoft sources (SSSs). Approximately 60 per cent of the population can be classified as XRBs, although there is source contamination from background AGN in this category as they have similar spectral shapes in the X-ray regime. Fifteen sources have X-ray colours consistent with SNRs, three of which correlate with known SNR/HII radio sources. Another two are promising new candidates for SNRs, one is unidentified, and the remainder are a mixture of foreground stars, bright soft XRBs and AGN candidates. We also detect 14 candidate SSSs, with significant detections in the softest X-ray band (0.3–1 keV) only. Sixteen sources display short-term variability during the *XMM-Newton* observation, twelve of which fall into the XRB category, giving additional evidence of their accreting nature. Using archival *Chandra* & *ROSAT* HRI data, we find that  $\sim 40$  per cent of the *XMM* sources show long-term variability over a baseline of up to  $\sim 10$  years, and eight sources display potential transient behaviour between observations. Sources with significant flux variations between the *XMM* and *Chandra* observations show a mixture of softening and hardening with increasing luminosity. The spectral and timing properties of the sources coincident with M101 confirm that its X-ray source population is dominated by accreting XRBs.

## Key words:

galaxies: individual (M101) – galaxies: spiral – X-rays: galaxies – X-rays: binaries

## 1 INTRODUCTION

Since the launch of the *Einstein* X-ray observatory in the late 1970’s, we have known that discrete, point-like X-ray sources form a major constituent of the overall X-ray output of spiral galaxies, along with hot diffuse gas and in some cases an active galactic nucleus (AGN) (e.g. Fabbiano 1989). There are a variety of compact sources that emit with sufficient luminosity in the X-ray regime to be observable in nearby galaxies. These include accreting sources, such as black hole/neutron star X-ray binaries (XRBs) and supersoft sources (SSSs), plus bright thermal supernova remnants (SNRs).

While *Einstein*, and later *ROSAT*, provided a preliminary

view of the X-ray source populations of nearby galaxies (e.g. Fabbiano & Trinchieri 1987; Read, Ponman, & Strickland 1997; Roberts & Warwick 2000), these studies were hindered by a lack of both spatial resolution and photon collecting area, leading to source confusion and limited spectroscopic capabilities. Now, with the current generation of X-ray observatories, *XMM-Newton* and *Chandra*, substantial progress is being made in this field. The sub-arcsecond spatial resolution of *Chandra* has led to up to a factor 100 increase in the number of sources detected in many galaxies. For example, the recent *Chandra* survey of 11 nearby spirals of Kilgard et al. (2004) has resolved on average 75 point sources per galaxy, with luminosities extending down to  $5 \times 10^{36}$  erg s<sup>-1</sup>. The luminosity functions derived from *Chandra* studies have also demonstrated that the overall X-ray emission in spiral/star-forming galaxies are typically dominated by a few bright extra-nuclear

\* E-mail: lej@star.le.ac.uk

sources (e.g. Kilgard et al. 2002; Colbert et al. 2004), the brightest of which are the ultraluminous X-ray sources (ULXs) with luminosities  $\geq 10^{39}$  erg s $^{-1}$  (see Miller & Colbert 2004 for a recent review). The complementary high throughput and large  $\sim 30$  arcminute field-of-view of *XMM-Newton* can be used for detailed spectral and variability studies of the brightest point sources in nearby galaxies. This has been demonstrated to great effect in the first paper in this series (Jenkins et al. 2004, hereafter Paper I), as well as the studies of M33 (Pietsch et al. 2004) and the archetypal starburst galaxy NGC 253 (Pietsch et al. 2001).

The target for this study is M101, a nearby ( $d=7.2$  Mpc, Stetson et al. 1998) grand-design spiral galaxy similar in morphological type to our own Milky Way. Its full face-on aspect and relatively low line-of-sight Galactic hydrogen column ( $N_H \sim 1.2 \times 10^{20}$  cm $^{-2}$ , Dickey & Lockman 1990) makes it an ideal laboratory for the study of the X-ray emission from compact discrete sources in spiral galaxies. M101 was first studied at X-ray energies with *Einstein* (McCammon & Sanders 1984; Trinchieri, Fabbiano & Romaine 1990), revealing X-ray emission associated with the nuclear region and HII regions in the spiral arms. Subsequent *ROSAT* studies revealed the presence of numerous discrete sources (Wang, Immler & Pietsch 1999) as well as a substantial diffuse component (Snowden & Pietsch 1995). More recently, a *Chandra* observation has revealed  $> 100$  discrete sources in the central  $\sim 8$  arcminutes of the galaxy (Pence et al. 2001; Mukai et al. 2003), as well as diffuse emission tracing the spiral arms (Kuntz et al. 2003).

This is the second of a series of papers on the *XMM-Newton* observation of M101. In Paper I, we presented the spectral and timing properties of the most luminous X-ray sources at the time of the *XMM-Newton* observation, many of which were in the ULX regime, and showed properties consistent with high-state XRBs. In this paper, we present the global properties of the complete set of X-ray sources detected within the spatial extent of M101 in the *XMM-Newton* observation, complemented with an analysis of two archival sets of *Chandra* observations of M101. An analysis of the diffuse X-ray emission will be presented in Paper III (Warwick et al., *in preparation*).

This paper is set out as follows. In section 2 we outline the observation details and data reduction techniques. In section 3 we detail the source detection techniques used, and the full source list is presented in section 4. In section 5 we broadly classify the sources according to their X-ray colours, and in section 6 we search for short-term variability within the *XMM-Newton* observation, and long-term source variability using archival X-ray observations. In section 7, we discuss the properties of the various source types, and in section 8 we summarise our results.

## 2 OBSERVATIONS & DATA REDUCTION

M101 was observed with *XMM-Newton* for 42.8 ks on the 4th June 2002 (ObsID 0104260101). The EPIC MOS-1, MOS-2 & PN cameras were operated with medium filters in ‘Prime Full Window’ mode, which utilizes the full  $\sim 30$  arcminute field of view of *XMM-Newton*, covering the entire D<sub>25</sub> ellipse of M101 ( $\sim 28.8$  arcminutes diameter, de Vaucouleurs et al. 1991). The data were pipeline-processed using the SAS (*Science Analysis Software*) v5.3.2 and all subsequent data analysis was carried out using SAS v5.4.1.

In this study we have performed source detection on both the PN and MOS data (see section 3). To increase the sensitivity of the MOS data, the MOS1 and MOS2 event lists were merged to-

gether using the SAS task MERGE. For the purposes of multi-band source detection (see section 3), images were created in the following three energy bands: 0.3–1 keV (soft), 1–2 keV (medium) and 2–6 keV (hard). The data were filtered using patterns corresponding to single & double pixel events for the PN (0 & 1–4), and patterns 0–12 (single to quadruple events) for the MOS cameras, together with the #XMMEA\_EM (MOS) and #XMMEA\_EP (PN) flags to remove hot pixels or out-of-field events. Full-field lightcurves were accumulated for the three exposures to check for high background intervals of soft proton flares. There were numerous small flares throughout the exposure. For the MOS data, we screened out time intervals corresponding to the four most prominent peaks with count rates greater than  $\sim 15$  counts per second, leaving a net good time for each camera of 36.7 ks. In the case of the PN data, inspection of the hard band (2–6 keV) images showed a greater contamination from flaring. In order to maximise the sensitivity of the data to the source detection algorithms, we further cleaned the data by selecting good time intervals (GTIs) corresponding to less than 0.9 counts per second (10–15 keV) in the single pattern lightcurve, leaving a net good time for the PN data of 25.7 ks.

As in Paper I, this dataset is supplemented with two archival *Chandra* observations of M101. These consist of one long ( $\sim 100$  ks) observation performed on the 26th March 2000 (ObsID 934), plus a short ( $\sim 10$  ks) observation performed on the 29th October 2000 (ObsID 2065). Though the first analysis of the central ACIS-S3 chip in the long observation is presented in Pence et al. (2001), we have used the analysis of both data sets presented in Kilgard et al. (2004) to search for long-term spectral and flux source changes. This analysis utilizes more up-to-date calibration files and includes sources from five ACIS chips, covering a larger fraction (78 per cent) of the D<sub>25</sub> ellipse of M101.

## 3 SOURCE DETECTION TECHNIQUES

We have performed multi-band source detection on EPIC images in the following energy bands; soft (0.3–1 keV), medium (1–2 keV) and hard (2–6 keV). Note that we have chosen to exclude data above 6 keV due to the relative domination of background components at these high energies. From the filtered images described in the previous section, exposure maps were created for each band using the SAS task EEXPMAP, and detector masks were created for each camera with EMASK to define the areas of the images suitable for source detection.

The key stages of source detection are the recognition of sources and their subsequent parameterization. The recognition stage can be performed using either a box or a wavelet detection algorithm. The standard SAS source searching routine implements the sliding box algorithm EBOXDETECT, which simultaneously searches the three energy band images for significant sources using a  $5 \times 5$  pixel window with a local background determined in a frame around the search box. However, for this study we have also chosen to implement the SAS source detection task EWAVELET, which searches for sources in single energy bands by convolving the input images with a circularly symmetric Mexican Hat wavelet function. This method is generally more efficient at separating close sources in confused areas such as the central region of M101, where the situation is further complicated by the presence of a substantial diffuse component.

Two sets of preliminary source lists were created for the PN and MOS using the two different methods (box and wavelet) as the initial source recognition stage, using first-order background

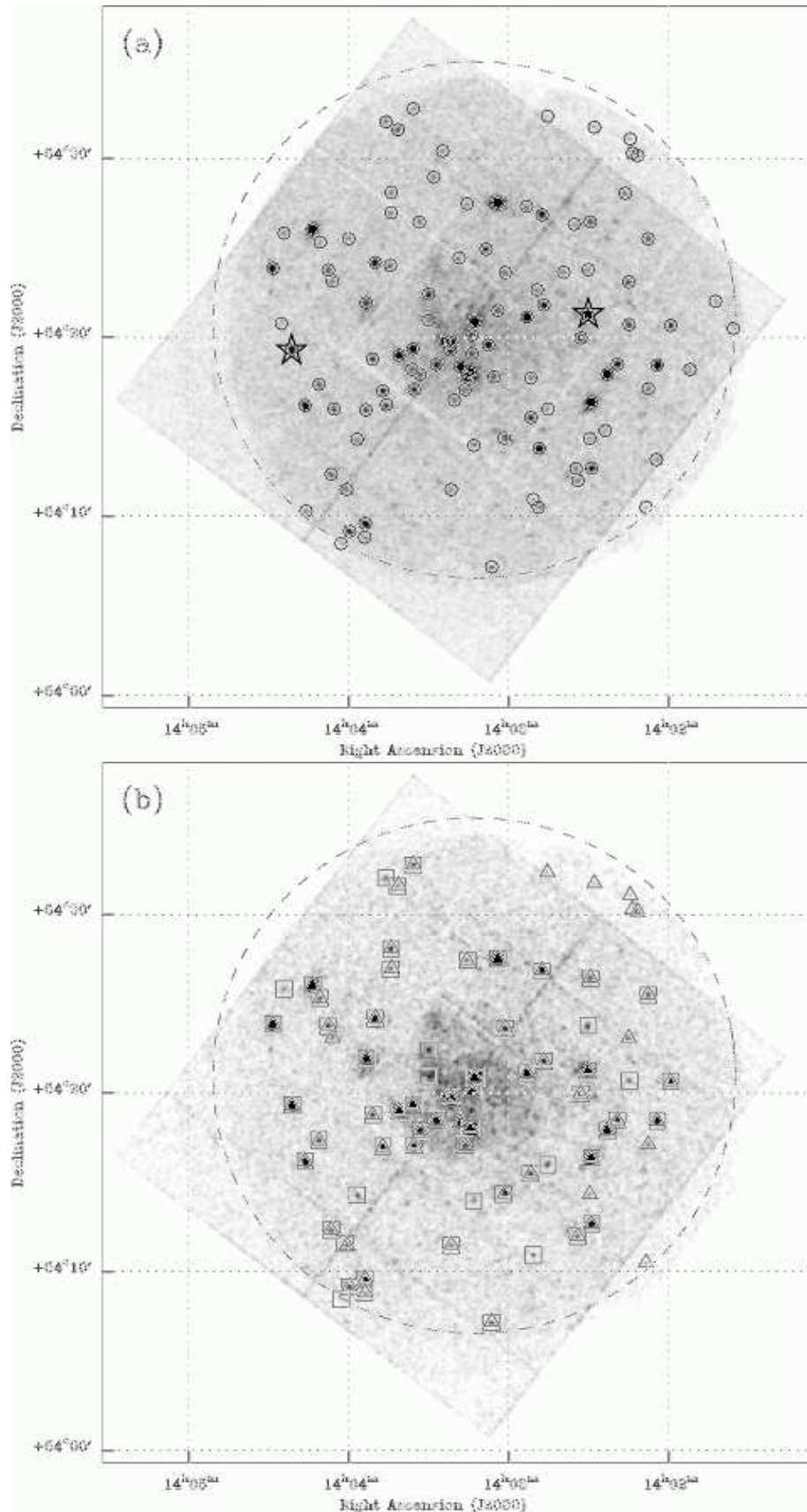


**Figure 1.** *XMM* EPIC images of the M101 field (stacked MOS & PN). (a) full sourcelist overlaid on a broad-band (0.3–6 keV) image. The two bright foreground stars in the field (#25 & 105) are marked with open star symbols. (b) soft (0.3–1 keV) image with significant soft sources. PN and MOS detections are denoted with squares and triangles respectively. The D<sub>25</sub> circle is shown with a dashed line.

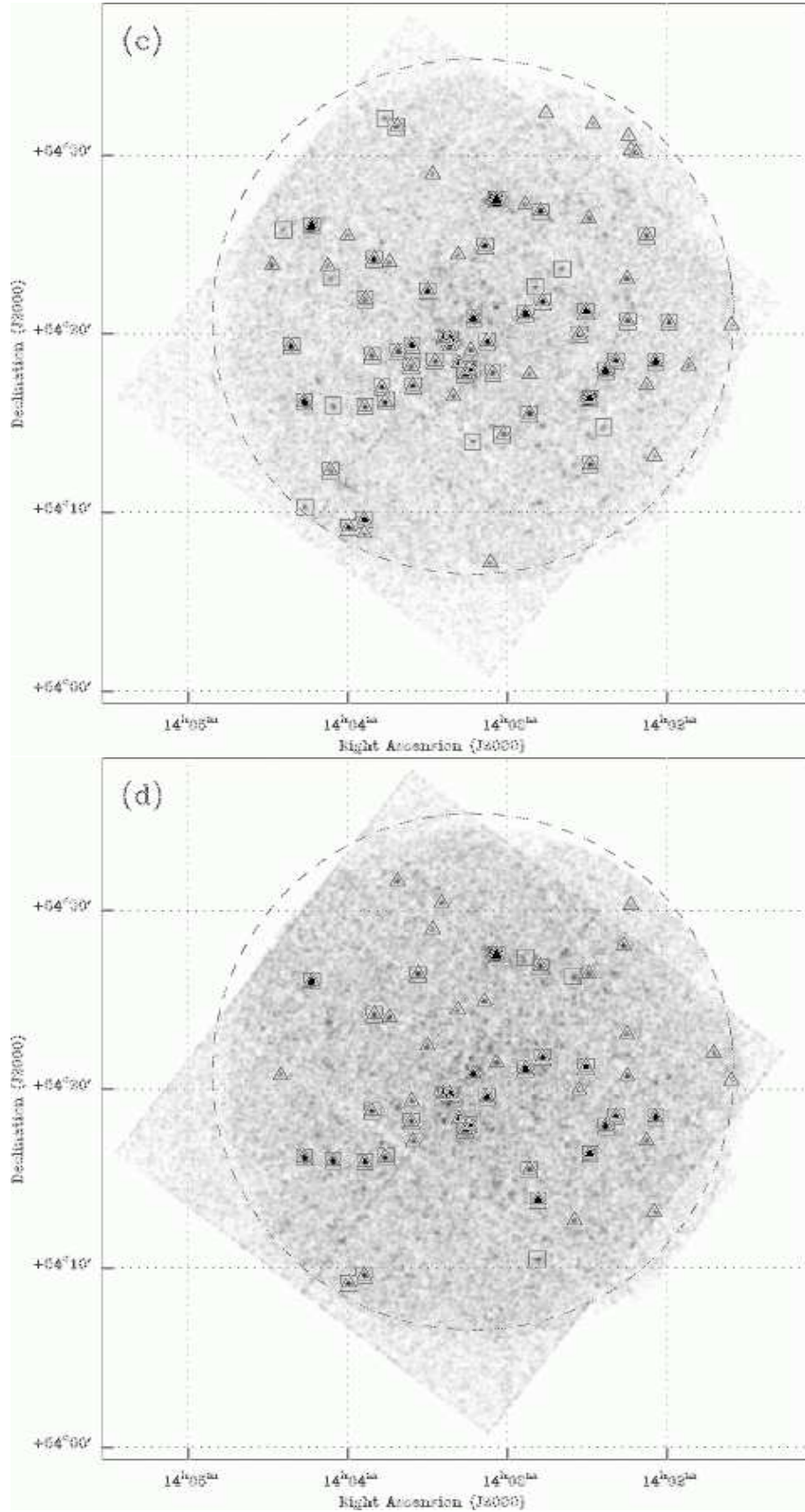


**Figure 1 – continued** (c) medium (1–2 keV) image with significant medium detections. (d) hard (2–6 keV) image with significant hard detections. PN and MOS detections are denoted with squares and triangles respectively. The D<sub>25</sub> circle is shown with a dashed line.

**Table 1.** M101 Source Catalogue.

Src	XMMU	$r_{1\sigma}$ ( $''$ )	PN count rate (count $\text{ks}^{-1}$ )			MOS count rate (count $\text{ks}^{-1}$ )			$F_X$	$L_X$	HR1	HR2	Var
			S	M	H	S	M	H					
(1)	(2)	(3)	(4)	(5)	(6)	(7)	(8)	(9)	(10)				
1	J140134.7+542031	2.05	-	-	-	0.3±0.2	<b>1.3±0.2</b>	<b>1.1±0.3</b>	2.28±0.41	1.42±0.25	0.59±0.18	-0.09±0.15	
2	J140141.3+542202	2.43	-	-	-	0.3±0.2	<b>0.5±0.2</b>	<b>1.0±0.2</b>	1.72±0.34	1.07±0.21	0.25±0.33	0.34±0.20	
3	J140151.1+541814	2.20	0.6±0.5	2.0±0.6	1.4±0.7	0.1±0.1	<b>0.9±0.2</b>	0.2±0.2	0.87±0.21	0.54±0.13	0.75±0.17	-0.41±0.18	L
4	J140158.4+542042	1.72	<b>7.0±1.0</b>	<b>3.4±0.7</b>	0.9±0.5	<b>0.9±0.2</b>	<b>1.0±0.2</b>	0.6±0.2	1.69±0.21	1.05±0.13	-0.18±0.09	-0.38±0.13	
5	J140203.5+541828	1.56	<b>9.7±1.1</b>	<b>10.8±1.1</b>	<b>5.7±0.9</b>	<b>3.1±0.3</b>	<b>3.3±0.4</b>	<b>2.8±0.3</b>	6.34±0.35	3.93±0.22	0.05±0.05	-0.18±0.06	S,L
6	J140203.9+541312	1.89	0.5±0.5	1.9±0.6	1.7±0.7	0.3±0.2	<b>0.7±0.2</b>	<b>1.0±0.2</b>	1.58±0.26	0.98±0.16	0.47±0.22	0.08±0.14	
7	J140206.8+542532	1.73	<b>3.0±0.7</b>	<b>2.1±0.6</b>	0.8±0.5	<b>0.7±0.1</b>	<b>0.8±0.2</b>	0.4±0.2	1.20±0.19	0.75±0.12	-0.01±0.11	-0.37±0.16	
8	J140206.9+541710	1.92	1.8±0.5	1.2±0.5	1.4±0.5	<b>0.6±0.1</b>	<b>0.7±0.2</b>	<b>0.8±0.2</b>	1.50±0.19	0.93±0.12	-0.04±0.13	0.11±0.13	
9	J140207.9+541033	2.14	-	-	-	<b>1.1±0.2</b>	0.8±0.2	0.7±0.3	1.75±0.43	1.08±0.26	-0.21±0.19	-0.06±0.27	
10	J140210.6+543011	1.72	-	-	-	<b>3.5±0.4</b>	<b>1.7±0.3</b>	0.2±0.2	2.58±0.36	1.60±0.22	-0.34±0.09	-0.78±0.19	
11	J140212.6+543019	2.04	-	-	-	<b>1.0±0.2</b>	<b>1.2±0.2</b>	<b>1.1±0.2</b>	2.43±0.35	1.51±0.22	0.10±0.15	-0.04±0.13	
12	J140213.5+543107	2.10	-	-	-	<b>0.7±0.2</b>	<b>0.7±0.2</b>	0.5±0.2	1.30±0.35	0.81±0.22	0.03±0.18	-0.20±0.27	
13	J140214.1+542045	1.81	<b>2.1±0.5</b>	<b>2.3±0.5</b>	1.9±0.5	0.3±0.1	<b>0.6±0.1</b>	<b>0.9±0.2</b>	1.61±0.19	1.00±0.12	0.18±0.12	0.08±0.11	L
14	J140214.3+542308	1.86	-	-	-	<b>0.5±0.1</b>	<b>1.1±0.2</b>	<b>0.6±0.1</b>	1.49±0.22	0.92±0.14	0.32±0.12	-0.29±0.14	
15	J140215.4+542085	1.97	-	-	-	0.1±0.1	0.5±0.2	<b>1.4±0.2</b>	2.13±0.32	1.32±0.20	0.72±0.32	0.50±0.14	
16	J140218.6+541832	1.66	<b>4.5±0.7</b>	<b>2.6±0.5</b>	<b>2.3±0.6</b>	<b>0.8±0.1</b>	<b>1.4±0.2</b>	<b>1.3±0.2</b>	2.51±0.22	1.56±0.13	0.04±0.08	-0.04±0.08	
17	J140222.4+541758	1.54	<b>14.6±1.1</b>	<b>10.2±0.9</b>	<b>5.7±0.8</b>	<b>3.2±0.3</b>	<b>3.8±0.3</b>	<b>1.9±0.2</b>	5.91±0.28	3.66±0.18	-0.07±0.04	-0.31±0.05	L
18	J140223.2+541450	3.16	0.3±0.4	<b>1.6±0.4</b>	0.7±0.4	-	-	-	0.68±0.25	0.42±0.16	0.68±0.33	-0.40±0.28	
19	J140227.1+541346	1.96	-	-	-	<b>0.9±0.2</b>	<b>1.1±0.2</b>	0.7±0.2	1.80±0.31	1.12±0.19	0.09±0.14	-0.22±0.17	S
20	J140228.4+541625	1.52	<b>22.9±1.3</b>	<b>34.0±1.6</b>	<b>13.9±1.1</b>	<b>5.1±0.4</b>	<b>10.4±0.5</b>	<b>7.1±0.5</b>	16.03±0.48	9.94±0.30	0.26±0.03	-0.31±0.03	S,L
21	J140228.5+541244	1.61	<b>11.5±1.1</b>	<b>3.0±0.6</b>	1.7±0.6	<b>2.7±0.3</b>	<b>1.2±0.2</b>	0.0±0.1	1.95±0.18	1.21±0.11	-0.50±0.06	-0.76±0.11	L
22	J140228.7+542629	1.78	<b>3.5±0.7</b>	1.2±0.4	2.0±0.6	<b>0.6±0.1</b>	<b>0.8±0.1</b>	<b>0.8±0.2</b>	1.67±0.20	1.04±0.12	-0.16±0.10	0.08±0.12	L
23	J140229.1+541424	2.34	-	-	-	<b>0.6±0.1</b>	0.5±0.1	0.1±0.1	0.53±0.15	0.33±0.09	-0.13±0.18	-0.79±0.34	
24	J140229.5+542349	2.07	<b>9.0±1.8</b>	0.0±0.7	0.2±0.5	-	-	-	1.08±0.37	0.67±0.23	-1.00±0.14	1.00±7.81	L
25	J140229.8+542118	1.51	<b>62.5±2.1</b>	<b>17.4±1.1</b>	<b>2.6±0.5</b>	<b>12.7±0.5</b>	<b>6.9±0.4</b>	<b>1.3±0.2</b>	10.70±0.27	6.64±0.17	-0.47±0.02	-0.70±0.03	S,L
26	J140232.4+542001	1.68	<b>1.9±0.5</b>	<b>2.2±0.4</b>	1.2±0.4	<b>0.6±0.1</b>	<b>1.0±0.1</b>	<b>0.5±0.1</b>	1.35±0.14	0.84±0.09	0.17±0.09	-0.28±0.10	
27	J140233.6+542023	1.97	<b>2.8±0.6</b>	0.8±0.4	0.8±0.5	<b>0.8±0.2</b>	0.6±0.2	0.6±0.2	1.09±0.20	0.68±0.13	-0.36±0.14	0.00±0.21	
28	J140234.3+541244	2.33	-	-	-	0.2±0.1	0.5±0.2	<b>1.0±0.2</b>	1.69±0.29	1.05±0.18	0.52±0.28	0.29±0.17	
29	J140234.8+542622	3.42	0.3±0.4	0.0±0.1	<b>3.4±0.9</b>	-	-	-	1.92±0.48	1.19±0.30	-1.00±0.96	1.00±0.08	L
30	J140238.8+542340	2.15	1.1±0.4	<b>1.4±0.3</b>	1.1±0.4	-	-	-	0.94±0.23	0.58±0.14	0.14±0.21	-0.13±0.21	L
31	J140244.9+541602	2.09	<b>3.0±0.5</b>	0.1±0.2	0.0±0.3	-	-	-	0.33±0.16	0.21±0.10	-0.96±0.11	-1.00±9.59	
32	J140244.9+542244	2.26	-	-	-	<b>0.9±0.2</b>	<b>0.7±0.2</b>	0.1±0.1	0.85±0.21	0.53±0.13	-0.16±0.16	-0.72±0.30	L
33	J140246.4+542151	1.60	<b>3.1±0.5</b>	<b>2.6±0.4</b>	<b>2.7±0.5</b>	<b>0.7±0.1</b>	<b>1.1±0.1</b>	<b>1.0±0.1</b>	2.21±0.17	1.37±0.10	0.08±0.08	-0.02±0.07	
34	J140247.0+542653	1.60	<b>19.4±3.2</b>	<b>11.2±2.4</b>	<b>8.2±2.4</b>	<b>1.5±0.2</b>	<b>1.0±0.2</b>	<b>0.6±0.1</b>	2.07±0.21	1.28±0.13	-0.23±0.08	-0.20±0.10	L
35	J140248.2+541351	1.62	0.6±0.4	1.1±0.3	<b>8.0±0.9</b>	0.1±0.1	0.2±0.1	<b>3.5±0.3</b>	4.81±0.34	2.99±0.21	0.32±0.24	0.82±0.05	L
36	J140248.5+541033	2.79	1.3±0.5	1.9±0.6	<b>2.6±0.7</b>	-	-	-	1.90±0.38	1.18±0.23	0.20±0.24	0.17±0.19	
37	J140248.9+542242	1.98	0.1±0.2	<b>1.1±0.3</b>	0.6±0.3	0.1±0.1	0.6±0.2	0.5±0.2	0.62±0.15	0.38±0.09	0.79±0.22	-0.18±0.19	
38	J140250.4+541100	1.83	<b>3.6±0.6</b>	0.0±0.2	0.0±0.1	-	-	-	0.39±0.09	0.25±0.06	-1.00±0.09	0.00±0.00	
39	J140251.3+541534	1.66	<b>2.3±0.5</b>	<b>2.0±0.4</b>	<b>1.5±0.4</b>	<b>0.7±0.1</b>	<b>1.0±0.2</b>	<b>0.8±0.1</b>	1.63±0.16	1.01±0.10	0.08±0.09	-0.12±0.10	
40	J140251.4+541747	2.01	1.3±0.4	0.5±0.3	0.7±0.3	0.2±0.1	<b>0.4±0.1</b>	0.1±0.1	0.49±0.11	0.30±0.07	-0.07±0.17	-0.26±0.21	
41	J140252.8+542111	1.54	<b>4.7±0.6</b>	<b>5.9±0.6</b>	<b>4.3±0.6</b>	<b>1.3±0.2</b>	<b>2.3±0.2</b>	<b>1.7±0.2</b>	3.88±0.21	2.41±0.13	0.19±0.06	-0.15±0.05	S,L
42	J140252.9+542721	1.94	2.1±1.5	3.0±1.5	<b>8.0±2.3</b>	0.3±0.1	<b>0.4±0.1</b>	0.1±0.1	0.49±0.15	0.30±0.09	0.20±0.19	0.09±0.18	
43	J140301.0+542340	2.07	<b>3.0±0.6</b>	0.0±0.1	0.0±0.1	<b>0.6±0.1</b>	0.0±0.0	0.0±0.1	0.31±0.07	0.19±0.04	-1.00±0.03	-1.00±4.95	L
44	J140301.4+541426	2.32	<b>19.8±2.9</b>	<b>7.6±1.8</b>	1.1±1.3	<b>1.2±0.2</b>	<b>0.6±0.1</b>	0.0±0.0	0.81±0.10	0.51±0.06	-0.40±0.08	-0.95±0.12	
45	J140303.8+542133	2.02	-	-	-	0.1±0.1	0.3±0.1	<b>0.6±0.1</b>	1.04±0.18	0.65±0.11	0.50±0.38	0.36±0.16	L
46	J140303.9+542734	1.51	<b>46.0±1.9</b>	<b>66.4±2.2</b>	<b>50.9±2.0</b>	<b>9.7±0.5</b>	<b>22.0±0.7</b>	<b>19.5±0.7</b>	41.98±0.79	26.04±0.49	0.28±0.02	-0.09±0.02	S,L
47	J140305.2+541751	1.78	1.5±0.5	<b>1.8±0.4</b>	0.5±0.3	0.2±0.1	<b>0.5±0.1</b>	0.3±0.1	0.72±0.11	0.45±0.07	0.24±0.14	-0.37±0.14	
48	J140306.2+540714	1.86	<b>4.7±0.9</b>	1.8±0.6	1.5±0.7	<b>1.5±0.3</b>	<b>1.3±0.3</b>	0.4±0.3	1.75±0.28	1.08±0.18	-0.23±0.11	-0.34±0.18	
49	J140307.4+541937	1.63	0.6±0.3	<b>2.1±0.4</b>	<b>3.1±0.5</b>	0.2±0.1	<b>0.8±0.1</b>	<b>1.4±0.2</b>	2.29±0.18	1.42±0.11	0.60±0.13	0.23±0.07	L
50	J140308.3+542458	1.68	1.2±0.4	<b>2.6±0.4</b>	1.4±0.4	0.2±0.1	<b>0.8±0.1</b>	<b>0.5±0.1</b>	1.22±0.13	0.76±0.08	0.45±0.11	-0.25±0.10	L
51	J140312.4+542056	1.55	<b>11.7±1.4</b>	<b>4.9±0.9</b>	1.6±0.6	<b>3.2±0.3</b>	<b>2.4±0.2</b>	<b>1.3±0.2</b>	3.87±0.22	2.40±0.14	-0.22±0.05	-0.33±0.06	S,L
52	J140312.9+541401	2.03	<b>1.8±0.4</b>	<b>1.6±0.4</b>	1.3±0.4	-	-	-	1.18±0.25	0.73±0.15	-0.06±0.17	-0.09±0.19	
53	J140313.6+542010	1.79	<b>4.9±0.7</b>	0.0±0.0	0.0±0.1	<b>1.0±0.1</b>	0.0±0.1	0.0±0.0	0.47±0.06	0.29±0.04	-1.00±0.02	1.00±23.56	L
54	J140313.6+541909	2.11	-	-	-	0.3±0.1	<b>0.5±0.1</b>	0.1±0.1	0.57±0.15	0.35±0.09	0.20±0.20	-0.55±0.24	
55	J140314.3+541806	1.50	<b>65.8±2.0</b>	<b>39.2±0.3</b>	<b>20.1±1.2</b>	<b>17.7±0.6</b>	<b>9.7±0.2</b>	-	27.44±0.37	17.02±0.23	-0.19±0.01	-0.29±0.01	S,L
56	J140315.4+542730	2.13	<b>2.4±0.5</b>	0.0±0.1	0.2±0.3	<b>0.4±0.1</b>	0.2±0.1	0.0±0.1	0.32±0.10	0.20±0.06	-0.89±0.10	-0.35±0.62	L
57	J140315.8+541747	1.59	0.0±0.2	<b>2.3±0.2</b>	<b>3.0±0.5</b>	0.0±0.1	<b>0.7±0.2</b>	<b>1.0±0.1</b>	1.70±0.13	1.05±0.08	1.00±0.12	0.15±0.08	L
58	J140316.3+541708	2.25	<b>2.4±0.5</b>	0.2±0.2	0.2±0.2	<b>0.6±0.1</b>	0.0±0.0	0.1±0.1	0.39±0.10	0.24±0.06	-0.93±0.11	0.51±0.64	L
59	J140318.1+541825	1.69	-	-	-	<b>1.0±0.2</b>	<b>1.1±0.2</b>	<b>0.9±0.1</b>	2.22				

**Table 1 – continued**

Src	XMMU	$r_{1\sigma}$ ( $''$ )	PN count rate (count $\text{ks}^{-1}$ )			MOS count rate (count $\text{ks}^{-1}$ )			$F_X$	$L_X$	HR1	HR2	Var
			S	M	H	S	M	H					
(1)	(2)	(3)	(4)	(5)	(6)	(7)	(8)	(9)	(10)				
76	J140336.3+541815	1.88	0.0±0.2	<b>1.6±0.4</b>	<b>1.6±0.4</b>	0.0±0.1	<b>0.5±0.1</b>	<b>0.5±0.1</b>	1.00±0.14	0.62±0.09	0.91±0.18	0.04±0.12	
77	J140341.2+541902	1.65	<b>9.5±0.9</b>	<b>2.8±0.5</b>	1.2±0.4	<b>2.5±0.3</b>	<b>0.8±0.1</b>	0.5±0.1	2.14±0.16	1.33±0.10	-0.53±0.05	-0.31±0.11	S
78	J140341.8+543138	1.75	<b>2.8±0.7</b>	<b>3.8±0.8</b>	1.9±0.8	<b>0.5±0.2</b>	<b>1.1±0.2</b>	<b>1.2±0.2</b>	2.21±0.27	1.37±0.17	0.26±0.11	-0.07±0.11	L
79	J140344.3+542808	1.88	<b>4.3±0.7</b>	0.0±0.2	0.0±0.3	<b>0.8±0.2</b>	0.1±0.1	0.1±0.1	0.52±0.13	0.32±0.08	-0.95±0.08	-0.14±0.70	
80	J140344.3+542700	2.01	<b>2.1±0.5</b>	1.1±0.4	0.8±0.5	<b>0.5±0.1</b>	0.1±0.1	0.4±0.2	0.81±0.18	0.50±0.11	-0.41±0.16	0.11±0.25	
81	J140344.5+542403	1.79	1.0±0.4	0.9±0.3	1.3±0.4	0.2±0.1	<b>0.8±0.2</b>	<b>0.8±0.1</b>	1.32±0.16	0.82±0.10	0.33±0.15	0.07±0.12	
82	J140345.9+541617	1.68	1.7±1.3	<b>8.9±1.9</b>	<b>9.0±2.1</b>	0.2±0.1	<b>1.0±0.2</b>	<b>1.1±0.2</b>	2.25±0.25	1.40±0.15	0.63±0.13	0.04±0.09	
83	J140346.4+543204	2.03	<b>4.9±1.0</b>	<b>3.8±0.9</b>	1.8±0.8	-	-	-	2.12±0.47	1.32±0.29	-0.12±0.16	-0.36±0.22	
84	J140347.3+541704	1.67	<b>5.2±0.7</b>	<b>2.1±0.5</b>	1.2±0.4	<b>1.1±0.2</b>	<b>0.8±0.1</b>	0.3±0.1	1.36±0.16	0.85±0.10	-0.29±0.08	-0.38±0.14	
85	J140350.3+542413	1.61	<b>7.7±0.8</b>	<b>3.1±0.5</b>	<b>2.3±0.5</b>	<b>1.3±0.2</b>	<b>1.4±0.2</b>	<b>0.6±0.1</b>	2.16±0.18	1.34±0.11	-0.26±0.07	-0.32±0.09	L
86	J140351.2+541850	1.65	<b>2.1±0.5</b>	<b>1.8±0.4</b>	<b>1.6±0.5</b>	<b>0.8±0.1</b>	<b>0.6±0.1</b>	<b>0.7±0.1</b>	1.50±0.17	0.93±0.10	-0.11±0.10	0.03±0.12	
87	J140353.7+542159	1.94	<b>7.2±0.8</b>	<b>1.5±0.4</b>	0.5±0.4	<b>1.5±0.2</b>	<b>0.7±0.1</b>	0.0±0.1	1.06±0.13	0.66±0.08	-0.55±0.07	-0.80±0.19	L
88	J140353.7+541559	1.75	0.5±0.3	<b>1.9±0.4</b>	<b>3.3±0.6</b>	0.0±0.1	<b>0.8±0.2</b>	<b>1.3±0.2</b>	2.13±0.23	1.32±0.14	0.81±0.16	0.24±0.09	
89	J140353.9+540939	1.58	<b>7.2±1.0</b>	<b>9.4±1.1</b>	<b>4.6±0.9</b>	<b>3.4±0.5</b>	<b>4.7±0.6</b>	<b>2.4±0.4</b>	5.66±0.42	3.51±0.26	0.15±0.06	-0.34±0.07	
90	J140354.0+540853	1.86	<b>3.4±0.9</b>	2.2±0.7	0.5±0.6	<b>1.3±0.3</b>	<b>1.5±0.3</b>	0.1±0.2	1.24±0.25	0.77±0.15	-0.02±0.11	-0.76±0.20	S
91	J140357.0+541421	1.77	<b>12.3±2.0</b>	0.9±0.8	2.0±1.2	-	-	-	2.59±0.71	1.61±0.44	-0.86±0.11	0.36±0.46	L
92	J140359.7+540913	1.65	<b>7.2±1.2</b>	<b>5.7±1.0</b>	<b>4.7±1.0</b>	<b>2.1±0.4</b>	<b>3.5±0.5</b>	<b>2.1±0.4</b>	4.82±0.43	2.99±0.27	0.10±0.08	-0.19±0.09	L
93	J140400.4+542533	2.02	1.3±0.5	1.4±0.5	1.0±0.5	0.2±0.1	<b>0.7±0.1</b>	0.1±0.1	0.68±0.16	0.42±0.10	0.28±0.17	-0.42±0.20	
94	J140400.9+541132	1.94	<b>6.4±1.6</b>	2.6±1.2	0.0±1.1	<b>1.6±0.3</b>	1.0±0.3	0.5±0.3	1.64±0.37	1.02±0.23	-0.30±0.12	-0.37±0.27	
95	J140402.9+540831	2.51	<b>3.9±1.0</b>	0.7±0.6	0.9±0.7	-	-	-	1.05±0.44	0.65±0.27	-0.70±0.23	0.15±0.57	
96	J140405.7+541602	1.74	0.0±0.1	<b>2.2±0.5</b>	<b>5.9±0.9</b>	0.2±0.1	0.6±0.2	<b>1.9±0.3</b>	3.25±0.30	2.02±0.19	0.98±0.07	0.48±0.08	
97	J140406.5+542310	2.03	1.6±0.5	<b>2.0±0.5</b>	1.8±0.6	<b>0.8±0.1</b>	0.3±0.1	0.1±0.1	0.90±0.18	0.56±0.11	-0.17±0.15	-0.10±0.19	
98	J140406.7+541223	1.77	<b>3.8±0.8</b>	<b>2.5±0.7</b>	1.6±0.6	<b>1.3±0.2</b>	<b>1.2±0.3</b>	0.7±0.3	1.86±0.27	1.16±0.17	-0.11±0.11	-0.24±0.15	
99	J140408.1+542347	1.75	<b>4.5±0.7</b>	1.5±0.5	1.7±0.6	<b>1.3±0.2</b>	<b>0.7±0.2</b>	0.8±0.2	1.82±0.24	1.13±0.15	-0.40±0.10	0.05±0.15	
100	J140411.3+542521	2.05	<b>3.6±0.7</b>	0.6±0.5	0.1±0.3	<b>0.8±0.2</b>	0.0±0.1	0.0±0.1	0.42±0.11	0.26±0.07	-0.89±0.11	-0.65±0.71	L
101	J140411.4+541724	1.86	<b>4.4±0.7</b>	1.1±0.4	1.2±0.5	<b>1.1±0.3</b>	0.9±0.3	0.6±0.3	1.43±0.25	0.88±0.16	-0.43±0.11	-0.09±0.20	
102	J140414.1+542604	1.51	<b>63.8±2.8</b>	<b>40.8±2.3</b>	<b>12.3±1.4</b>	<b>15.6±0.8</b>	<b>14.7±0.8</b>	<b>4.9±0.5</b>	20.10±0.61	12.47±0.38	-0.14±0.03	-0.52±0.03	S,L
103	J140416.2+541020	2.48	2.2±0.8	<b>2.8±0.8</b>	1.4±0.8	-	-	-	1.49±0.48	0.92±0.30	0.14±0.23	-0.32±0.28	
104	J140416.7+541614	1.56	<b>12.7±1.2</b>	<b>11.5±1.1</b>	<b>7.3±1.0</b>	<b>4.9±0.5</b>	<b>4.4±0.5</b>	<b>3.5±0.5</b>	7.98±0.47	4.95±0.29	-0.05±0.05	-0.17±0.06	S,L
105	J140421.7+541921	1.57	<b>25.0±1.7</b>	<b>5.8±0.8</b>	0.8±0.5	<b>5.0±0.5</b>	<b>2.4±0.4</b>	0.5±0.2	4.01±0.26	2.49±0.16	-0.54±0.04	-0.71±0.09	S,L
106	J140425.0+542550	2.08	<b>2.9±0.8</b>	<b>2.6±0.7</b>	1.3±0.7	-	-	-	1.44±0.42	0.90±0.26	-0.06±0.19	-0.32±0.27	
107	J140425.8+542047	4.73	-	-	-	0.1±0.1	0.4±0.2	<b>1.0±0.2</b>	1.62±0.33	1.00±0.21	0.50±0.37	0.41±0.22	
108	J140429.1+542353	1.62	<b>23.3±1.8</b>	2.1±0.5	0.0±0.3	<b>5.9±0.6</b>	<b>1.4±0.3</b>	0.1±0.1	3.05±0.22	1.89±0.13	-0.78±0.03	-0.92±0.16	L

(1) source number; (2) XMMU source designation (J2000 coordinates); (3)  $1\sigma$  error radius (including a 1.5 arcsecond systematic error); (4 & 5) source count rates in soft (0.3–1 keV), medium (1–2 keV) & hard (2–6 keV) bands for the PN and MOS cameras, with the significant source detections ( $> 4\sigma$ ) highlighted in bold; (6) source flux in units of  $10^{-14}$  erg  $\text{cm}^{-2}$   $\text{s}^{-1}$  in the broad (0.3–6 keV) band; (7) source luminosity in units of  $10^{38}$  erg  $\text{s}^{-1}$  in the 0.3–6 keV band (assuming a distance to M101 of 7.2 Mpc); (8 & 9) soft (HR1) and hard (HR2) hardness ratios (as defined in the text); (10) X-ray variable on short (S) and long (L) time-scales.

maps created with ESPLINEMAP. Both sets of sourcelists were then parameterized with EMLDETECT, which performs maximum likelihood instrumental point spread function (PSF) fits to the source count distributions. In the case of the sliding box detection method, this was performed simultaneously in the three energy bands, whereas the PSFs were fitted separately for each band with the wavelet method. All sources were treated as point sources, i.e. no source extent was fitted. Since the background is high in the EPIC instruments and the PSF wings extensive, we chose to improve the modeling of the background using the SAS task ASMOOTH, which adaptively smoothes the source-subtracted background images to a signal-to-noise ratio of 30. We ran ASMOOTH and EMLDETECT two times each on both sets of sourcelists, with the aim of improving the source parameterization with each iteration. The source detection threshold was set using a limiting likelihood (DET<sub>ML</sub>) of 11, which corresponds to a detection probability of  $4\sigma$  for a three-band detection. However, sources were only deemed to be significant if they reached a  $4\sigma$  single-band detection threshold (DET<sub>ML</sub>=10) in at least one of the three energy bands, and all sources not fulfilling this criterion were rejected.

The two sets of sourcelists were then compared, and any additional sources detected with Ewavelet were added to the EBOXDETECT input list. The source parameterization process was then repeated to ensure a consistent multi-band parameterization for all sources detected by both methods. At a  $4\sigma$  detection threshold, we expect  $\sim 6$  spurious sources in the combined EPIC

sourcelist due to statistical background fluctuations (i.e.  $\sim 1$  for each of the three energy band for both PN and MOS). To eliminate these, each source was visually inspected simultaneously in each detector in each energy band, and those which were deemed to be spurious (or at chip edges) were removed. In addition, sources falling outside of the D<sub>25</sub> ellipse of M101 were rejected. The source count rates and fluxes were determined by EMLDETECT, using the exposure maps to correct for vignetting and losses due to chip gaps and bad pixels/columns. To convert the count rates to fluxes, we computed energy conversion factors (ECFs) in WEBSPEC for each energy band assuming a simple power-law spectral shape with  $\Gamma=1.7$  and Galactic absorption ( $N_H \sim 1 \times 10^{20}$  cm $^{-2}$ ). Finally, the PN and MOS sourcelists were merged into a summary sourcelist with the SAS task SRCMATCH. Two detections of a source were merged if their positions matched to within their  $3\sigma$  errors (comprised of both a statistical error plus a 1 arcsecond systematic error).

#### 4 SOURCE CATALOGUE

In total, 108 sources were detected within the D<sub>25</sub> ellipse of M101 in the *XMM* EPIC data. The source parameters are listed in Table 1 as follows: (1) source number, (2) XMMU designation, (3)  $1\sigma$  error radius including both the statistical error and a systematic error of 1.5 arcseconds added in quadrature, (4 & 5) count rates in the soft

**Table 2.** M101 source cross-identifications.

Src	<i>ROSAT</i> ID <sup>a</sup> HRI(H)/PSPC(P)	Pence <sup>b</sup>	<i>Chandra</i> ID Kilgard <sup>c</sup>	Other
1	P3	-	-	[PMC2001] RX J140134.94+542029.2 Galaxy
2	-	-	-	
3	-	-	-	GSC1251 Star
4	-	-	-	
5	H3/P4	-	J140203.6+541830	XMM-8
6	-	-	-	
7	-	-	J140206.8+542534	
8	H4	-	-	
9	H5	-	-	
10	H6/P5	-	-	[WIP] AGN
11	-	-	-	
12	-	-	-	
13	-	-	-	
14	H8	-	J140214.1+542310	
15	-	-	J140214.8+542804	
			[J140217.0+542803]	
16	-	-	J140218.9+541833	
17	H9/P6	-	J140222.2+541756	XMM-6
18	-	-	-	
19	-	-	-	
20	H10/P8	-	J140228.3+541626	XMM-4, NGC 5447, [TFR] 2, [HK83, HGGK] HII
21	H11/P7	-	-	[WIP] Star
22	H12	-	J140228.7+542632	
23	-	-	-	
24	-	-	-	
25	H13/P9	-	J140229.9+542119	GSC1275 Star
26	H14	-	J140232.5+542002	
27	-	-	-	
28	-	-	-	
29	-	-	-	
30	-	-	J140238.9+542344	
31	-	-	-	
32	-	-	J140245.2+543221	
33	H16	-	J140246.4+542152	
34	H17/P10	-	J140247.0+542656	[WIP] Galaxy
35	-	-	-	
36	-	-	-	
37	-	-	J140249.1+542241	
38	-	-	-	
39	-	-	-	
40	-	-	J140251.5+541748	[MF] 22 SNR, [HGGK] HII
41	H18/P11	5	J140252.9+542112	XMM-12
42	-	-	J140252.9+542719	
43	-	13	J140301.2+542342	
44	P12	-	-	NGC 5455, [HK83] HII, SN1970G
45	-	17	J140303.9+542133	
46	H19/P13	-	-	XMM-1, [MF] 37 SNR, [TFR] 5
47	-	19	J140305.2+541753	
48	H21/P14	-	J140306.1+540713	
49	-	25	J140307.4+541938	
		[21]	[J140306.0+541945]	
50	-	29	J140308.4+542459	
51	H23/P16	40	J140312.5+542057	XMM-10 (nucleus), [CC2002] HII
		38	J140312.5+542053	
52	-	-	-	
53	H24	45	J140313.6+542010	[CC2002] HII
54	-	47	J140313.7+541909	[HGGK, H69] HII
		[42]	[J140312.8+541901]	[MF] 46 SNR (= P42)
55	H25/P17 [H22]	51	J140314.3+541807	XMM-2, [H69] HII
		[48]	[J140313.9+541811]	
56	-	-	-	GSC0731 Star
57	-	57	J140315.8+541749	[H69] HII
58	-	-	-	[HK83, HGGK] HII

**Table 2 – continued**

Src	ROSAT ID <sup>a</sup> HRI(H)/PSPC(P)	Pence <sup>b</sup>	Chandra ID Kilgard <sup>c</sup>	Other
59	H26	63 [60] [62]	J140318.1+541823 [J140316.8+541835] [J140317.7+541836]	
60	H27	64	J140318.7+542430	
61	-	66	J140320.3+541633	
62	-	-	-	
63	H29/P19 [H30]	70 [67]	J140321.5+541946 -	XMM-9, [HGGK] HII [MF] 54 SNR (= P67)
64	-	71 [68]	J140321.7+541920 [J140321.2+541908]	
65	H30/P19 [H29]	76	J140324.2+541949	XMM-14, [HK83,HGGK] HII
66	-	-	J140325.1+543026	[IGA75] 22 Radio source
67	-	85	J140327.1+541832	[MF] 65 SNR, [HK83] HII
68	-	-	J140328.3+542858	
69	-	92 [90]	J140329.9+542058 [J140328.9+542059]	
70	-	93 [94]	J140330.0+542229 [J140330.7+542222]	[BKS96] Star cluster
71	H33	99	J140333.3+541760	[CC2002] HII
72	-	-	-	
73	H35	103	J140335.5+541709	
74	H36/P21	104	J140336.0+541925	XMM-11, [MF] 83 SNR, [LCC2001] Stars in MF83
75	-	-	-	
76	-	105	J140336.3+541816	
77	H37/P22	107	J140341.3+541904	XMM-13, NGC 5461, [HK83,HGGK] HII
78	P23	-	J140341.1+543138	[WIP] Star
79	-	-	J140344.9+542809	
80	-	-	J140344.7+542658	
81	-	-	J140344.9+542401	
82	-	-	J140346.2+541615	
83	-	-	J140346.5+543202	
84	-	-	J140347.5+541704	
85	H38/P24	-	J140350.6+542413	[WIP] AGN
86	-	-	J140351.3+541848	
87	H40/P25 [H39,H41]	110	J140354.0+542157 -	NGC 5462, [HK83,CasHII] HII, [ECB2002] $\theta$ Radio source
88	-	-	J140353.6+541558	
89	-	-	J140354.2+540938	[TFR] 6
90	-	-	J140354.1+540852	
91	-	-	J140357.5+541416	
92	H43/P26	-	J140359.3+540912	[WIP] AGN
93	-	-	J140400.5+542533	
94	H44/P27	-	J140400.8+541130	[WIP] AGN
95	-	-	-	
96	-	-	J140405.9+541602	
97	-	-	-	
98	-	-	J140406.9+541223	[TFR] 7
99	-	-	J140408.4+542347	
100	-	-	-	[S71] HII
101	-	-	J140411.8+541726	
102	H45/P28	-	J140414.3+542604	XMM-3, [TFR] 8
103	-	-	-	
104	H47/P30	-	J140416.8+541615	XMM-5, [PMC2001] RX J140416.61+541618.2 BLAGN
105	H48/P31	-	J140421.9+541920	GSC1069, [AG79] 10 Star
106	-	-	J140425.3+542555	
107	-	-	-	
108	H49/P32	-	J140429.1+542353	XMM-7, NGC5471, [CCG2002] NGC 5471B

Notes: <sup>a</sup>ROSAT ID numbers correspond to HRI (H) and PSPC (P) detections (Wang et al. 1999). <sup>b</sup>Chandra ID numbers from Pence et al. (2001)

<sup>c</sup>Chandra ID numbers from Kilgard et al. (2004). For (b) & (c), square brackets denote additional Chandra sources matched to within 15 arcseconds of the *XMM* positions. ‘NGC’ denotes giant HII regions e.g. Williams & Chu (1995). Catalogues references: [GSC] Guide Star Catalogue; [AG79] Allen & Goss (1979); [CasHII] Sanduleak & Pesch (1987); [BKS96] Bresolin, Kennicutt, & Stetson (1996); [CC2002] Cedrés & Cepa (2002); [CCG2002] Chen et al. (2002); [ECB2002] Eck, Cowan, & Branch (2002); [H69] Hodge (1969); [HGGK] Hodge et al. (1990); [HK83] Hodge & Kennicutt (1983); [IGA75] Israel, Goss, & Allen (1975); [LCC2001] Lai et al. (2001); [MF] Matonick & Fesen (1997); [PMC2001] Page, Mittaz, & Carrera (2001); [S71] Searle (1971); [TFR] Trinchieri et al. (1990); [WIP] Wang et al. (1999).

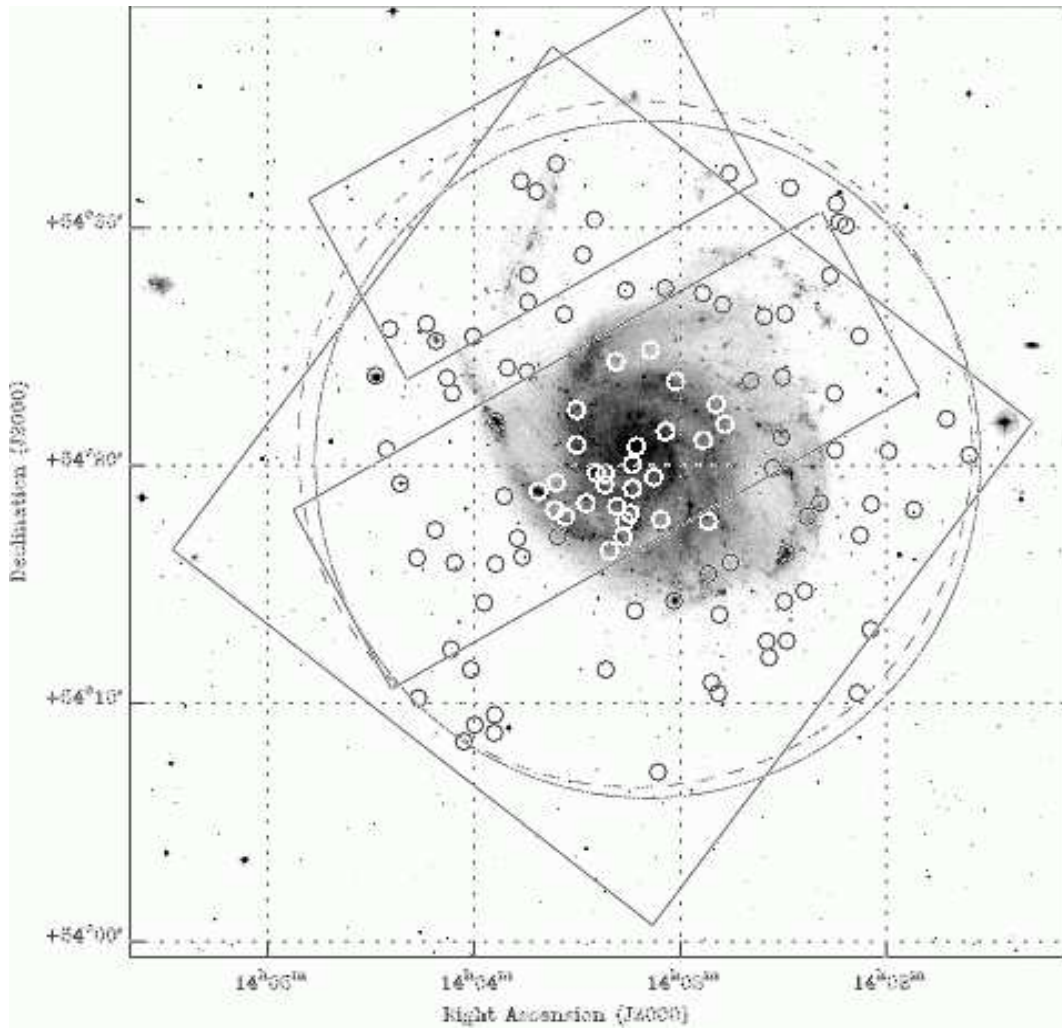


**Figure 2.** *XMM* source positions (circles) overlaid on a DSS2 optical blue image (note that source circles do not represent positional error radii). The large square and circular footprints denote the fields of view of the PN and MOS cameras respectively. The smaller rectangle footprints denote the fields of view of the ACIS-S and -I arrays in the 100 ks *Chandra* observation of March 2000. The  $D_{25}$  ellipse is shown with a dashed line.

(S), medium (M) and hard (H) bands in the PN and MOS cameras with significant band detections ( $> 4\sigma$ ) highlighted in bold, (6) flux in the 0.3–6 keV band, (7) luminosity in the 0.3–6 keV band assuming a distance to M101 of 7.2 Mpc, (8 & 9) soft (HR1) and hard (HR2) hardness ratios, (10) X-ray variability detected in the short- (S) and long- (L) term.

The broad-band (0.3–6 keV) fluxes quoted in column 6 were obtained by summing the fluxes over the three sub-bands and then taking the weighted mean of the individual PN and MOS measurements. The faintest source detected has a flux of  $3.1 \times 10^{-15}$  erg cm $^{-2}$  s $^{-1}$  in the 0.3–6 keV range, and the brightest source (#46/XMM-1) has a flux of  $4.2 \times 10^{-13}$  erg cm $^{-2}$  s $^{-1}$ . These correspond to a luminosity range of  $1.9 \times 10^{37}$ – $2.6 \times 10^{39}$  erg s $^{-1}$  at the distance of M101. In Figure 1, the full set of sources is plotted on a broad-band (0.3–6 keV) image EPIC of M101 (a), and separate images are shown for the soft (b), medium (c) and hard bands (d) with significant ( $> 4\sigma$ ) detections in those bands marked with squares (PN) and triangles (MOS). To illustrate the source positions with respect to the optical emission from M101, Figure 2 shows the source positions overlaid on a DSS2 blue image.

The hardness ratios shown in columns 8 & 9 are calculated directly from the source count rates measured in the source detection routines. They are defined as  $HR1 = (M-S)/(M+S)$  and  $HR2 = (H-M)/(H+M)$  where S, M & H denote the count rates in the three energy bands. In order to take advantage of the improved statistics, we quote the weighted mean EPIC (combined PN and MOS) ratios for sources detected in both cameras. For sources detected only in either the PN or MOS data, the single camera ratios are listed (see section 5 for further details).

#### 4.1 X-ray/multiwavelength cross-correlations

We have cross-correlated the *XMM* sourcelist with previous X-ray observations of M101 (see Table 2). For the *Chandra* observations detailed in section 2, we matched on-axis sources (whose positions are generally accurate to  $\sim 1$  arcsecond) to within the *XMM*  $3\sigma$  errors. For off-axis sources, the decreasing *Chandra* positional accuracy to  $\sim 2$  arcseconds was also taken into account. However, given the large PSF of *XMM* ( $\sim 6$  arcseconds FWHM), we have also checked for any contamination from additional fainter sources detected only by *Chandra* by searching for sources that lie within

**Table 3.** X-ray colour classifications for *XMM* EPIC observations in the 0.3–6 keV range (medium filter).

Classification	EPIC (PN & MOS)	Definition	
		PN only	MOS only
Supernova remnant	$HR1 < -0.24, HR2 < -0.10$	$HR1 < -0.34, HR2 < -0.14$	$HR1 < -0.15, HR2 < -0.07$
X-ray binary	$-0.24 < HR1 < 0.57, -0.8 < HR2 < 0.8$	$-0.34 < HR1 < 0.52, -0.8 < HR2 < 0.8$	$-0.15 < HR1 < 0.62, -0.8 < HR2 < 0.8$
Background source	$HR1 < -0.24, HR2 > -0.10$	$HR1 < -0.34, HR2 > -0.14$	$HR1 < -0.15, HR2 > -0.07$
Absorbed source	$HR1 > 0.57$	$HR1 > 0.52$	$HR1 > 0.62$
Indeterminate soft source	$-0.24 < HR1 < 0.57, HR2 < -0.8$	$-0.34 < HR1 < 0.52, HR2 < -0.8$	$-0.15 < HR1 < 0.62, HR2 < -0.8$
Indeterminate hard source	$-0.24 < HR1 < 0.57, HR2 > 0.8$	$-0.34 < HR1 < 0.52, HR2 > 0.8$	$-0.15 < HR1 < 0.62, HR2 > 0.8$

15 arcseconds of the *XMM* source positions (this corresponds to the on-axis 68 per cent energy cut-out radius used in EMLDETECT). In total, 71 *XMM* sources are unambiguously matched to single *Chandra* sources within the  $3\sigma$  errors, whereas the nuclear source is resolved into two sources by *Chandra*. These matches are listed in Table 2, and any additional sources matching to within 15 arcseconds are shown in square brackets. For completeness, we show both the CXOU designations of Kilgard et al. (2004) and equivalent source numbers from Pence et al. (2001).

The *ROSAT* HRI and PSPC X-ray detections of Wang et al. (1999) were matched to within the combined  $3\sigma$  *XMM* and *ROSAT* errors, and 38 matches were found. Where sources detected in the PSPC observation were confused with multiple HRI sources, the confused HRI sources are shown in square brackets. In addition, in the absence of any other multiwavelength identification, the optical counterpart identifications for several sources from Wang et al. (1999) are also included (denoted [WIP] in the final column of Table 2). The *Einstein* source detections of Trinchieri et al. (1990) (denoted [TFR]) are also shown in the final column.

To aid our identification of the X-ray sources, we have searched for multi-wavelength correlations in the NED and SIMBAD archives using a  $3\sigma$  search radius, and the results are also shown in the final column in Table 2. The XMM–n source designations of the bright sources in Paper I are also listed here. In addition, we have searched for matches to the 93 optical SNRs found in M101 by Matonick & Fesen (1997) (denoted [MF]), matching with the more accurate *Chandra* positions where available to within a combined 2 arcsecond error. Four matches were found; three using *Chandra* positions (*XMM* source numbers #40, 67 & 74), and one with the bright *XMM* source (#46/XMM-1) whose position matches that of MF37 to  $\sim 2$  arcseconds. We also list the matches between the faint *Chandra* source P67 (confused with #63/XMM-9) and MF54, whose positions correlate to within less than an arcsecond (as demonstrated by Snowden et al. 2001), plus the *Chandra* source J140312.8+541901 (confused with *XMM* source #54), which is coincident with MF46 to within  $\sim 1$  arcsecond.

Overall, 74 *XMM* sources are X-ray detections only. Of the remainder, 20 are coincident with HII and/or SNRs, 7 have identified/candidate background AGN/galaxy counterparts, 6 are coincident with foreground stars and one has a radio counterpart.

## 5 X-RAY COLOURS

In Paper I, we performed detailed spectral analyses of the fourteen brightest sources in the *XMM* field with sufficient counts for spectral fitting ( $> 300$  in the PN data). Here, we attempt to broadly classify the complete *XMM* source population according to their X-ray colours (hardness ratios). Although we cannot definitively classify any source by its X-ray colour alone, this approach can be a use-

ful starting point for source identification as well as giving insights into the overall source population of a galaxy.

We have used the X-ray colour classification scheme of Prestwich et al. (2003) and Kilgard et al. (2004), which was developed to classify *Chandra* point sources using the colours of known XRBs and SNRs. We have modified the scheme for *XMM* EPIC data, ensuring that the source categories cover the same spectral ranges as the *Chandra* scheme (Figure 3). The distribution in this colour space of sources detected with both PN and MOS (i.e. ‘EPIC’) with  $\Gamma=0.5\text{--}3$  and absorption values of  $N_H = 10^{20} - 5 \times 10^{22} \text{ cm}^{-2}$  is shown in Figure 3 (top left), with ellipses illustrating the upper and lower boundaries of the coarse colour ranges for different source categories (see Table 3 for details). For consistency with the data (see section 4), the EPIC power-law grid was calculated using the mean of the separate model PN and MOS hardness ratios at each point. The XRB range encompasses sources with spectral shapes equivalent to a power-law slope of  $\Gamma \sim 1\text{--}2.5$ , typical of low- and high-mass XRBs (Prestwich et al. 2003 and references therein), and the SNR range covers soft sources ( $\Gamma \gtrsim 2$ ) with low absorption, typical of the soft thermal spectra of known SNRs. The absorbed source range applies to sources with  $N_H \gtrsim 5 \times 10^{21} \text{ cm}^{-2}$ , and the background source range covers objects with complex two-component spectra with highly absorbed power-law continua and soft excesses.

In Figure 3 (top right) the X-ray colours of the sources detected in both the PN and MOS cameras are plotted. For sources detected only in either the PN or MOS data, we have plotted their separate hardness ratios with equivalent classification spectral ranges applicable to the PN and MOS responses in Figure 3 (bottom). In general, the sources detected by PN only are near MOS chip gaps/detector edges or are very soft sources as is shown in Figure 3 (bottom left). This higher sensitivity to soft sources is to be expected, as the PN camera has a much greater effective area at soft energies than the MOS cameras. For the MOS only sources (Figure 3, bottom right), the distribution of hardness ratios is more even, and they were generally not detected in the PN data because they were either outside the PN field of view or near PN chip gaps.

Since the sources are expected to (and indeed have) a variety of spectral shapes, they are not all detected significantly in all three energy bands. We have therefore plotted the sources in the X-ray colour plane using the following symbols: circle (TTT), box (TTF); triangle (FTT); star (TFF); cross (FTF); diamond (FFT) denoting sources detected (T) or not detected (F) significantly in the soft, medium and hard bands respectively. For this purpose, a  $3\sigma$  detection threshold is used (rather than the  $4\sigma$  used for source detection) to provide a better estimation of the intrinsic spectral shapes of the sources.

The sources are distributed among the four designated colour-colour categories as follows: 62 XRBs, 15 SNRs, 11 absorbed

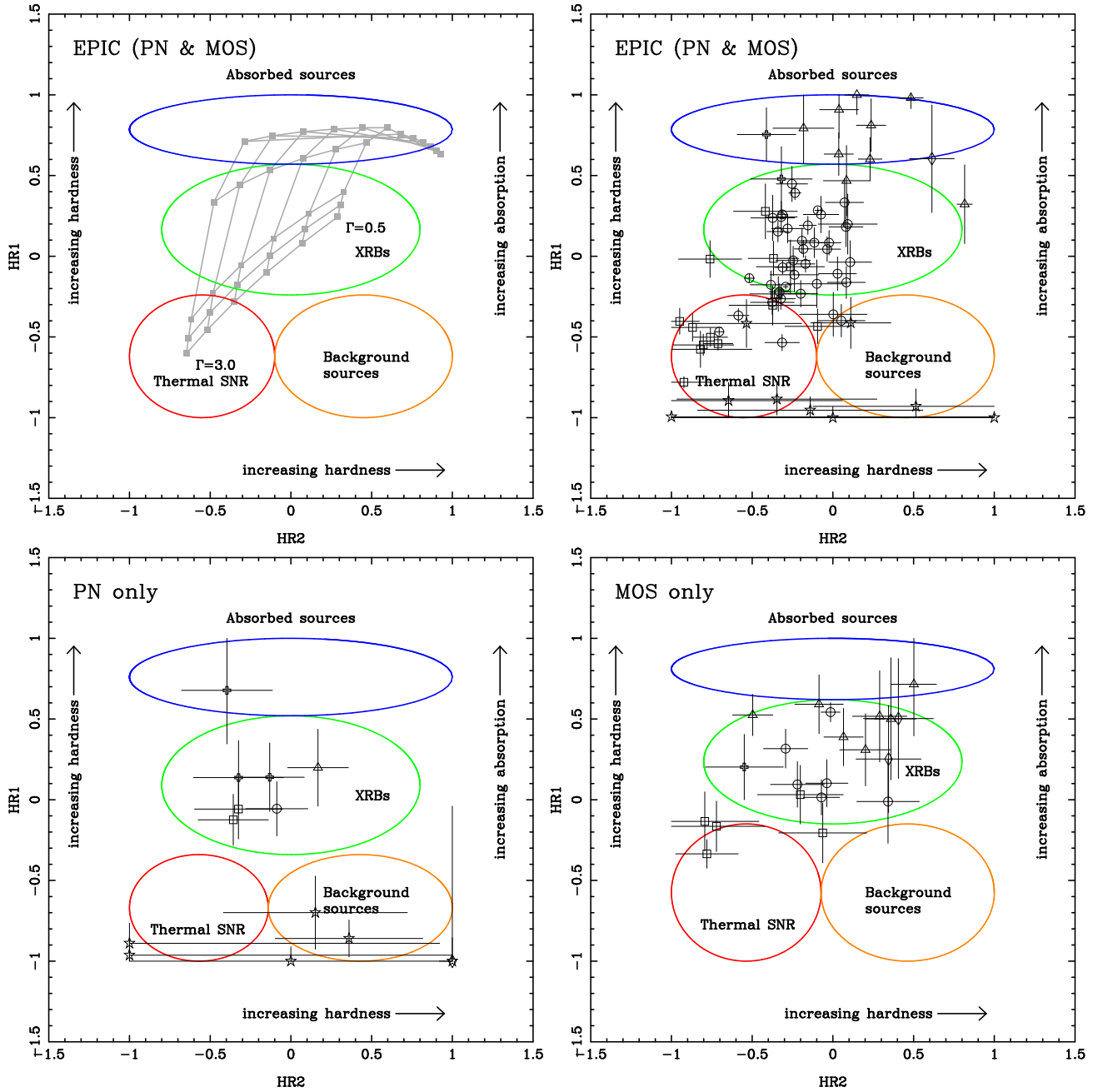


**Figure 3.** Upper left: *XMM* EPIC (PN & MOS) X-ray colour diagram showing the source classification scheme defined by Prestwich et al. (2003) and Kilgard et al. (2004). The ellipses illustrate the boundaries of the colour ranges for each category. The model grid shows  $N_H$  absorption values ranging between  $10^{20} - 5 \times 10^{22} \text{ cm}^{-2}$  (bottom to top) with photon indices ranging between  $\Gamma = 0.5 - 3.0$ . Upper right: *XMM* EPIC (PN & MOS) X-ray colours of the discrete sources in M101 detected with both cameras. The symbols denote true (T) or false (F) detections above the  $3\sigma$  detection threshold in the soft, medium and hard bands: circle (TTT), box (TTF); triangle (FTT); star (TFF); cross (FTF); diamond (FFT). Lower left: *XMM* PN only detections. Lower right: *XMM* MOS only detections.

sources and 5 background sources. In addition, there are 15 candidate SSSs i.e. sources only detected significantly in the soft band (see section 7.4). These are not included in any of the four categories, but appear at  $\text{HR1} \simeq -1$  (marked with stars in Figure 3). However, additional information such as source variability, position in the galaxy and multiwavelength counterparts should be taken into account when classifying sources, and each category is discussed in turn in section 7. In Figure 4, the positions of the sources are plotted on an HI map and an *XMM* Optical Monitor (OM) UV im-

age of M101, with colours denoting where the sources lie in the classification scheme.

## 6 TIMING PROPERTIES

### 6.1 Short-term variability

In Paper I, eleven of the fourteen brightest sources in the *XMM* observation were found to be variable at  $> 95$  per cent probability

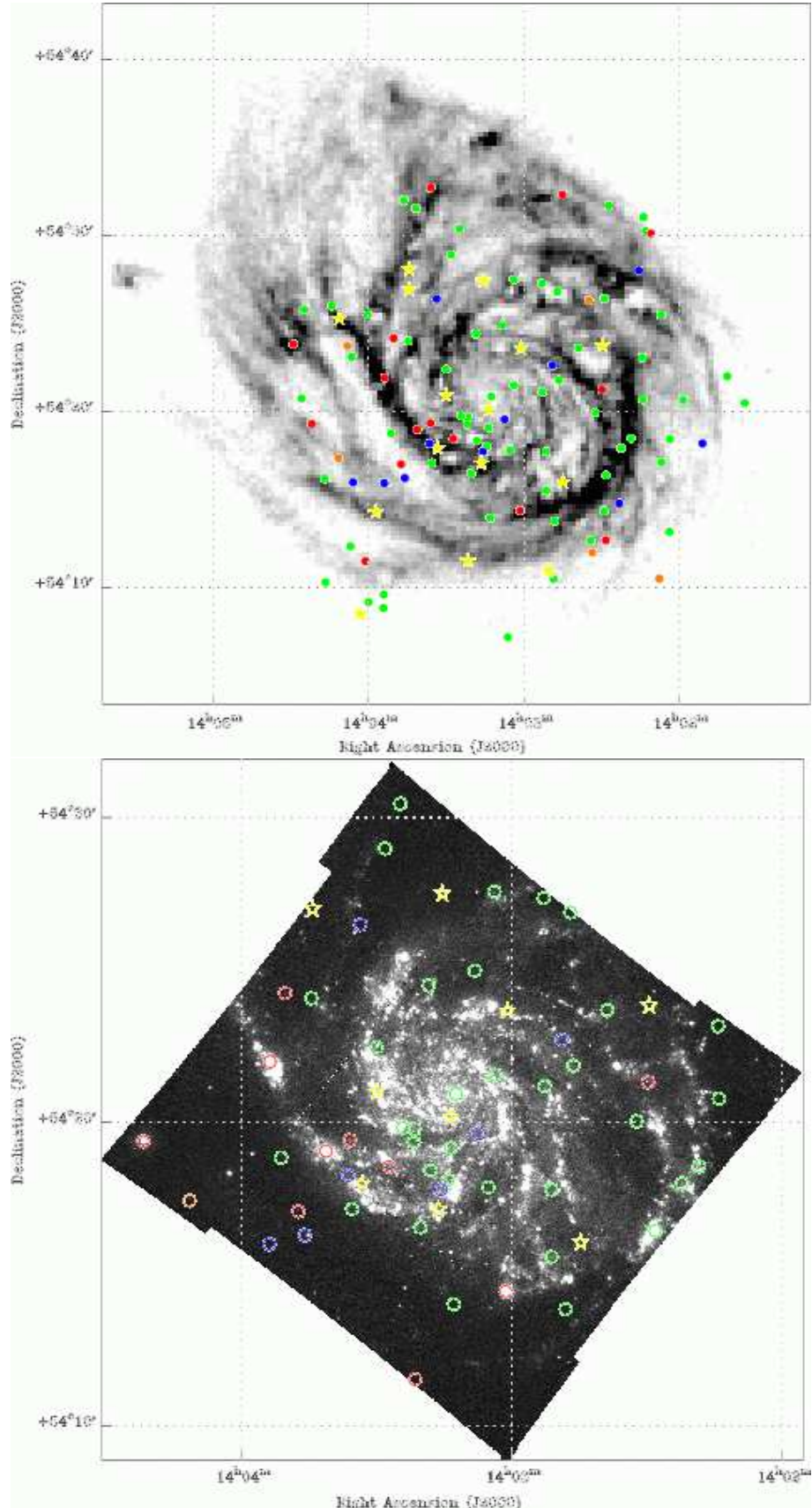


**Figure 4.** Top: *XMM* sources overlaid on an HI image of M101 from Kamphuis, Sancisi, & van der Hulst (1991). Bottom: *XMM* sources overlaid on an *XMM* OM UVW1 ( $\lambda_{\text{central}} = 2910 \text{ \AA}$ ) image of the central region of M101. The colours corresponding to the source classifications in the X-ray colour scheme, and candidate SSSs are marked with yellow stars.

using  $\chi^2$ , Kolmogorov-Smirnov (K-S) and standard deviation tests (see table 5, Paper I). For the majority of the remainder of the sources, we do not have sufficient counts for such detailed analyses. Instead, we have performed simple standard deviation tests in the following manner. Firstly, for consistency between the datasets and to filter out as much background variability as possible, the heavier time filter used in the PN source detection was applied to the MOS data. Sources were then divided into categories of 2, 4, 6 & 8 time bin resolutions depending on their total (background subtracted) counts (PN+MOS) detected during this period ( $\sim 26$  ks), ensuring at least 20 counts per bin for each source. Images were created for each time bin category using equally-spaced time intervals, and the source counts in each determined with EMLDETECT.

Fifty-one sources had sufficient counts for a 2 time-bin resolution only, and for these we compared the two values with their respective  $1\sigma$  errors. Of these, only two were variable above the 95 per cent level (# 19 at  $2.7\sigma$  & # 90 at  $2.8\sigma$ ). For the remaining sources with 4, 6 & 8 time bins, we calculated a standard deviation of the number of counts per bin from the mean, and compared this to the expected deviation of  $\sim 22$  per cent expected from Gaussian counting noise. Only three sources (# 25, 70 & 105) were variable at  $> 95$  per cent. As each had comparably high numbers of counts ( $> 200$ ), we confirmed their variability by extracting full short-term light-curves, again with time bin sizes tailored so so that each bin had at least 20 counts after background subtraction. Again, to minimize contamination from soft proton flaring, we applied the heavier time filtering to the data, and corrected the exposure times and count rates in incomplete bins with a simple scaling factor, excluding bins with  $<0.3$  times the exposure remaining of the original bin size. The resulting light curves are shown in Figure 5, and  $\chi^2$  tests showed each to be variable at greater than 99.73 per cent probability. Interestingly, two of these variable sources are the two bright foreground stars (# 25 & 105), which were excluded from our analyses in Paper I as they were not associated with M101 (see section 7.5 for further discussion). In total, 16 sources show short-term variability above the 95 per cent level in this dataset (including the variable bright sources from Paper I), which we denote with an 'S' in column 10 of Table 1.

## 6.2 Long-term variability

### 6.2.1 Long-term flux changes

To search for long-term source variability, we have compared the observed fluxes in the *XMM* observation with those measured in the *Chandra* observations conducted  $\sim 2$  years previously, plus four archival *ROSAT* HRI observations. The *ROSAT* observations span  $\sim 4$  years beginning in January 1992, giving a total baseline of  $\sim 10$  years for sources detected with both *ROSAT* and *XMM*. Twenty-three *XMM* sources were detected in at least one of the four HRI observations, thirteen of which are the bright sources analysed in Paper I. Since the HRI count rates quoted in Wang et al. (1999) are averages of the four individual observations, we have re-analysed the archival data sets (as per Roberts & Warwick 2000), measuring count rates (or upper limits) in the 0.5–2 keV band for each individual observation. Seventy one *XMM* sources are matched in the *Chandra* observations, ten of which are confused (or possibly confused) with nearby sources. Where sources were detected in both *Chandra* observations, the source counts from the longer observation were used to ensure the most accurate flux determinations. For consistency between the data sets, the measured count rates from the *Chandra* and *ROSAT* observations were converted into fluxes

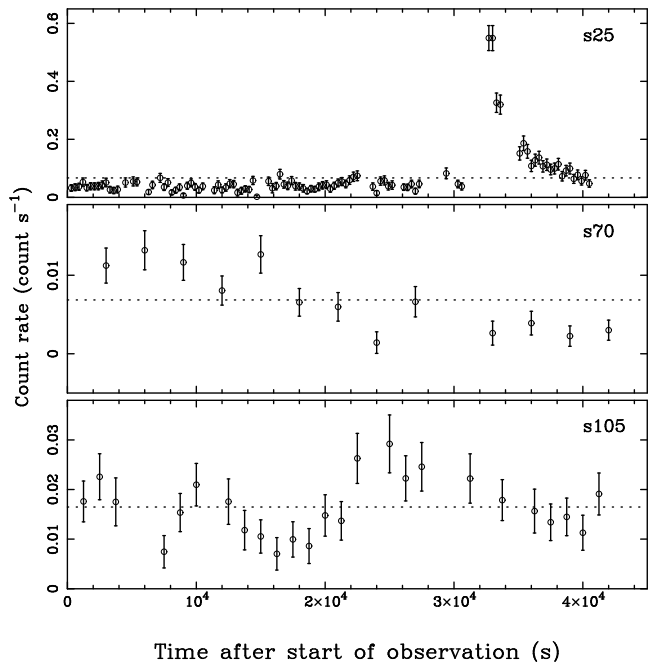


**Figure 5.** *XMM* short-term lightcurves for three variable sources (#25, 70 & 105), obtained by summing the counts from the 3 EPIC cameras. The mean count rates are shown as dashed lines and error bars correspond to  $1\sigma$  deviations assuming Gaussian statistics.

in the 0.3–6 keV band using ECFs determined from WebPIMMS, using the same spectral model used for the *XMM* flux conversions ( $\Gamma=1.7$ ,  $N_H=1 \times 10^{20} \text{ cm}^{-2}$ ).

To quantify this variability, we have compared the maximum to minimum observed fluxes of each source in this multi-mission data set. For the *XMM/ROSAT* sources shown to be confused by multiple source detections in the *Chandra* observations, flux changes were only deemed real in the *Chandra* data if the variability was only apparent using the flux of the source matching most closely to the *XMM* position, as opposed to the combined flux of the confused sources. In total, 37 sources show long-term variability at  $> 2\sigma$ , with 26 variable above the  $3\sigma$  level. The majority (32 of 37) vary by a factor of 1.5–4 between the highest and lowest observed fluxes. The most variable sources are #21, 53 & 87, which vary by factors of 6–8, and #56 (a foreground star), which is  $\sim 17$  times fainter than in a *ROSAT* observation in 1992. The most variable source we detect is #55/XMM-2 (see section 6.2.2 below).

In addition, 30 *XMM* sources have not been detected in any previous X-ray observation, and we have investigated whether this is due to real source variability as opposed to differing coverage and/or lack of photon sensitivity. Fourteen sources are covered by the two *Chandra* observations; the flux limits on the positions of four (#3, 13, 58 & 100) imply that they have all brightened by at least factors of 3–5 between the *Chandra* and *XMM* observations, while eight are at or below the detection thresholds at their positions. The remaining two sources (#24 & 29) are sufficiently variable to be classified as transients (see section 6.2.2 below). The whole field was covered in the *ROSAT* HRI observations, but all but one of the *XMM* sources with no HRI matches fall below the flux limit of the longest 108 ks HRI observation ( $F_X \sim 2.3 \times 10^{-14} \text{ erg cm}^{-2} \text{ s}^{-1}$ ,  $L_X \sim 1.4 \times 10^{38} \text{ erg s}^{-1}$ , extrapolated to the 0.3–6 keV band) and therefore cannot be classed as variable based on these data. The only exception is #35, which should have been detected in the both of the longest HRI obser-

vations. The flux limits of these observations imply an increase in luminosity of this source of at least a factor of  $\sim 2$  in the *XMM* observation.

In total, 44 *XMM* sources ( $\sim 40$  per cent of the source population) show long-term variability, either by direct measurement with detections at different epochs (at  $> 2\sigma$ ) or by the implied variations of the flux limits of the archival data. These are all denoted by ‘L’ in column 10 of Table 1.

### 6.2.2 Transient sources

Transient behaviour is characteristic of low-mass XRB (LMXB) systems, with observed outbursts believed to be caused by hydrogen-ionization instabilities in the accretion disc around the primary black hole/neutron star (see for example King 2002). Such outbursts do not generally occur in high-mass XRBs (HMXBs), as the companion star is a sufficient source of irradiation to keep the accretion disc in a stable ionized state (although it is possible that they could occur in HMXBs with Be-star companions, see King 2004). Galactic soft X-ray transients (SXTs) have quiescent X-ray luminosities in the  $10^{32} - 10^{34}$  erg s $^{-1}$  range (see e.g. Menou et al. 1999), and often increase by a factor of  $10^7$  or more in outburst (King 2004). Since such faint quiescent sources are beyond the flux limits of any existing X-ray observation of M101, we have searched for *candidate* transient sources by comparing the full *XMM* sourcelist with previous *Chandra* and *ROSAT* detections to ascertain lower limits on the flux variability of highly variable sources. For these purposes we define candidate transient sources as those varying by at least an order of magnitude.

The most obvious transient candidate detected in the *XMM* observation is #55/XMM-2, which has a luminosity a factor of  $\sim 30$  brighter than the flux level seen in previous observations (see Paper I). Another highly variable source is the most luminous ULX (P98) in the long *Chandra* observation (Mukai et al. 2003). It was initially detected in a *ROSAT* observation (H32), and increased in flux by a factor of  $\sim 5$  in the later *Chandra* observation. It then fell below the detection threshold in the *XMM* observation, implying another drop in luminosity of at least a factor of  $\sim 20$ . For an additional two *XMM* sources not detected by *Chandra*, the difference between their fluxes and the flux limits in the *Chandra* observations at those positions imply variability large enough to be classed as candidate transient behaviour. Source #24 with SSS X-ray colours shows a massive increase of a factor of at least  $\sim 580$  in the *XMM* observation, while #29 must have increased by a factor of at least  $\sim 20$ .

It is also worth noting that there are another four bright *ROSAT* HRI sources ( $L_X \gtrsim 10^{38}$  erg s $^{-1}$  in the 0.3–6 keV band) that are undetected in the *XMM* observation, suggesting transient behaviour. Two sources, H28 with a ULX luminosity of  $L_X \sim 10^{39}$  erg s $^{-1}$  in the first HRI observation, and H31 with  $L_X \sim 4 \times 10^{38}$  erg s $^{-1}$  in the second observation, are both undetected by *Chandra* and *XMM*. H15 is detected in the fourth HRI observation with  $L_X \sim 1.4 \times 10^{38}$  erg s $^{-1}$ , but is then detected with *Chandra* with a factor of  $\sim 5$  lower flux. Another source, H34, is detected in the combined HRI dataset by Wang et al. (1999), with an average luminosity of  $L_X \sim 1 \times 10^{38}$  erg s $^{-1}$ . Therefore, we identify eight candidate transient sources in total using these datasets.

### 6.2.3 Colour changes

Nineteen sources show variability at the  $3\sigma$  level between the *XMM* and *Chandra* observations, ten increasing and nine decreas-

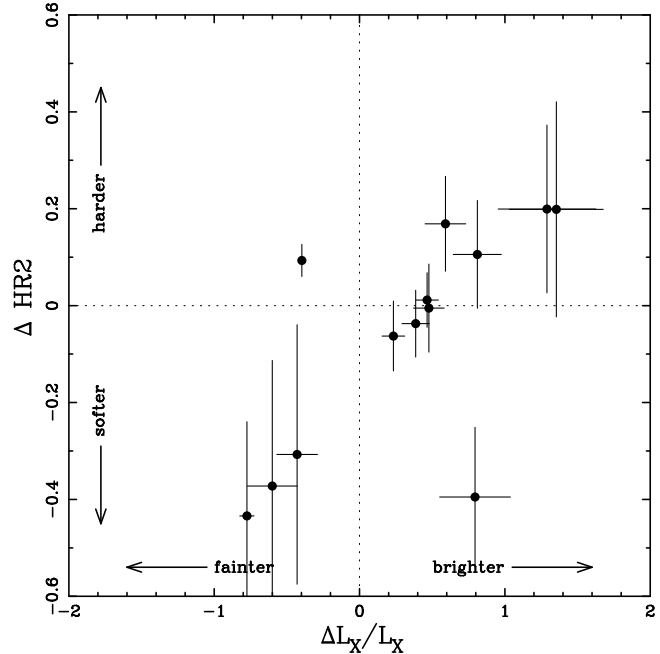


**Figure 6.** Plot of the change in hard X-ray colour ( $\Delta\text{HR2}$ ) versus the fractional change in luminosity [ $\Delta L_X/L_X = (L_X(\text{XMM}) - L_X(\text{Chan})) / L_X(\text{Chan})$ ] between the *Chandra* and *XMM* observations of M101.

ing in flux. Since XRBs and ULXs are known to undergo spectral transitions as their accretion rates change, we have compared the X-ray colours of these sources in both observations to search for such behaviour. To directly compare the source colours between the observations, correction factors were applied to the *Chandra* X-ray colours to account for the differences in energy response and effective area of the two telescopes. The correction factors were calculated as the differences in the soft and hard colours for representative average spectral models for XRBs ( $\Gamma=1.5$ ,  $N_H=10^{21}$  cm $^{-2}$ ), SNRs ( $\Gamma=3$ ,  $N_H=10^{20}$  cm $^{-2}$ ) and absorbed sources ( $\Gamma=1.5$ ,  $N_H=10^{22}$  cm $^{-2}$ ), and were applied depending on the source positions on the equivalent *Chandra* colour-colour plane.

Figure 6 shows the changes in the hard (HR2) X-ray colour versus the change in luminosity between the two observations as a fraction of the *Chandra* luminosity [ $\Delta L_X/L_X = (L_X(\text{XMM}) - L_X(\text{Chan})) / L_X(\text{Chan})$ ]. Note that we have not used the soft (HR1) colour to look for intrinsic colour changes, as this is much more sensitive to varying absorption within M101. The two foreground stars are not plotted in this diagram, nor do we plot the SSSs as their hard colours are unconstrained. The transient source (#55/XMM-2) is also excluded as its change in luminosity is far larger than the other sources ( $\Delta L_X/L_X \sim 32$ ) and it has no significant colour variation. Although these thirteen sources all show some shift in colour between the observations, all but two remain in the same spectral classification between the observations as expected. The exceptions are #20/XMM-4, which increases in flux between the *Chandra* and *XMM* observations, moving from the absorbed to the XRB class, and #87 located in the giant HII region NGC 5462, which decreases in flux and moves from the XRB to the SNR class (see section 7.3).

Interestingly, the majority of sources do not appear to follow the ‘canonical’ low/hard (LH) power-law dominated to high/soft (HS) disc-dominated state transitions seen in many Galactic black

hole binary systems (e.g. McClintock & Remillard 2004). Only four sources follow this pattern using the HR2 colour (#41/XMM-12, #65/XMM-14, #102/XMM-3 & #78), three of which are bright sources analysed in detail in Paper I. The remaining sources fall into the opposite quadrants where the fainter the source, the softer its spectrum and vice versa, and recent studies with *XMM-Newton* and *Chandra* have demonstrated that many bright ULXs do display this behaviour (e.g. Fabbiano et al. 2003; Dewangan et al. 2004; Roberts et al. 2004). Although there may be underlying physical reasons for this type of behaviour in XRBs (see for example Fabbiano et al. 2003), we must consider whether these results may partly be due to the X-ray energy bands covered by both *XMM-Newton* and *Chandra* in these studies (typically 0.3–10 keV). Indeed, when using the broader band 2–8 keV/0.3–2 keV flux ratio in Paper I, seven sources did show a typical softening with increasing luminosity. The main spectral states of XRBs have traditionally been defined using a much harder 2–20 keV energy range, covered by e.g. the Rossi X-ray Timing Explorer (*RXTE*, see McClintock & Remillard 2004). Since the sources in our sample have luminosities at  $\gtrsim 10^{38}$  erg s $^{-1}$ , they are possibly in disc-dominated states. If their inner disc temperatures are  $\sim 1$ –2 keV, they will contribute to the spectrum mainly at 1–6 keV. If the flux change is coming from the emergence of the disc relative to the power-law component, the spectrum can appear to get harder in the 1–2 keV range compared to the 2–6 keV range. Therefore, we could still be observing the classic power-law to disc state transition; however observations of large samples of XRBs in this wider X-ray spectral band will be needed to confirm whether this is the case.

## 7 SOURCE CLASSIFICATION

### 7.1 Background galaxies/AGN

We can estimate the probability of any of our detections being background sources using the hard-band (2–10 keV) integral  $\log(N)$ – $\log(S)$  relationship of Campana et al. (2001). We judge this to be a better indicator than the soft-band  $\log(N)$ – $\log(S)$  due to the high, spatially variable neutral absorption column associated with the disc of M101. A  $4\sigma$  source detection threshold in the hard 2–6 keV band corresponds to  $\sim 28$  counts in both the PN and MOS. After converting this into a 2–10 keV flux for a typical faint AGN ( $\Gamma=1.4$ ,  $N_H = 3 \times 10^{20}$  cm $^{-2}$ ), and folding this through both the exposure map for the observation (to correct for sensitivity changes across the EPIC field-of-view) and the 2–10 keV  $\log(N)$ – $\log(S)$ , we predict a total contamination of  $\sim 18$  background AGN in the PN data and  $\sim 24$  in the MOS.

Sources #1 & 104 have been optically identified as background galaxies in the *ROSAT* survey of hard sources of Page et al. (2001). We note that source #104 is one of the bright sources analysed in Paper I (XMM-5), where we omitted this optical identification as a broad-line AGN. It showed a composite X-ray spectrum comprised of a power-law plus a MEKAL thermal plasma, and we discussed the possibility that it was an XRB associated with M101 based on its positional coincidence with the end of a spiral arm and short- and long-term variability. However, these properties are also consistent with this source being a background galaxy with a thermal component from e.g. a supernova-driven galactic wind. A further five candidate AGN/background galaxies have also been identified by Wang et al. (1999) based on the colours of optical counterparts, although two of these (#10 & 94) are not significantly

detected in the hard 2–6 keV band. In addition, an interarm sources (#66) with hard X-ray colours has a radio counterpart, which points to it being a background radio galaxy.

In total, fifty-four sources are significantly detected ( $> 4\sigma$ ) in the hard 2–6 keV band. From an inspection of the positions of these sources with respect to optical DSS and HI images, approximately half are coincident with star forming HII regions or spiral arm structure, arguing that they are associated with M101. The remaining sources are the best candidates for background AGN, and are either interarm or sources located away from the main body of M101. This number is consistent with the number of background sources we expect based on the statistical arguments given above.

The majority of the hard sources fall into the XRB and absorbed source categories in the X-ray colour classification scheme. It is interesting to note that in Figure 4 (top), while the thermal SNR candidate sources (plotted in red) correlate well with the HI structure, many of the absorbed sources (plotted in blue) fall into interarm regions. The HI column in M101 ranges from  $\sim 1 \times 10^{20}$  cm $^{-2}$  in the interarm regions to  $\sim 10^{22}$  cm $^{-2}$  in the spiral arms (Braun 1995), which implies that interarm absorbed sources with  $N_H \gtrsim 10^{22}$  cm $^{-2}$  must possess absorption in excess of that in the disc of M101, indicating that they are likely to be background galaxies.

We note that the only source in the background source class to be significantly detected in the hard band is #29. However, apart from the some SSS candidates that lie in this region (see section 7.4), the remaining source classifications are ambiguous, as they are all borderline between the background source/XRB/SNR categories, with error bars that overlap these categories, and therefore cannot be firmly classified with this data.

### 7.2 X-ray binaries (XRBs)

The X-ray colours show that a large proportion of the *XMM* sources ( $\sim 60$  per cent) have spectral shapes consistent with XRBs. However, not all of these sources are associated with M101 itself. Again, from an inspection of the source locations with respect to the optical and HI images, we estimate that approximately half are associated with star-forming HII regions or spiral arm structure. As shown above in section 7.1, the majority of background AGN candidates also have X-ray colours in the same spectral range, and constitute the main contaminant in this category. Indeed, both of the optically identified background galaxies (#1 & 104), plus two of the five AGN candidates of Wang et al. (1999) fall into this category. In addition, absorbed or nonthermal emission from SNRs may also fall in this spectral range on the X-ray colour diagram.

Our detailed spectral and timing analyses of the fourteen brightest sources in this field in Paper I allows us to investigate the robustness of this classification scheme. Eleven of the fourteen sources are classed as XRBs in this scheme, which agrees with our interpretation (based on spectral shape and variability) of ten being high-state XRBs, and one being a (now identified) background AGN (#104/XMM-5). The three exceptions are XMM-7, XMM-11 & XMM-13, which fall into the thermal SNR range. However, this can be understood because their spectra were generally soft; XMM-7 is a SSS and XMM-11 and XMM-13 both have strong soft components in their spectra. This demonstrates that there is an overlap region between true SNRs and soft XRBs.

Additional evidence that the sources in this category are accreting systems comes from our detection of short-term variability during the *XMM* observation. Of the sixteen sources found to have statistical short-term variability at greater than the 95 per cent level,

twelve fall into the XRB category. The remaining four fall into the SNR category; however these are all sources separately identified as either stars or soft XRBs where variability on this timescale is expected (see section 7.3).

### 7.3 Supernova remnants (SNRs)

SNRs generally have soft thermal X-ray spectra with the majority of their flux below 2 keV (e.g. Pietsch et al. 2004). Fifteen sources fall into the SNR category in the X-ray colour classification scheme, although four show short-term X-ray variability that we would not expect to detect from SNRs. However, these four are all separately identified either as stars (#25 & 105) or bright soft XRBs (#74/XMM-11 [coincident with SNR MF83] & #77/XMM-13).

Of the eleven non-variable sources in this category, one is a star (#21), another is a bright soft XRB (#108/XMM-7) and three are optically identified AGN candidates (#10, #85 & 94, see section 7.1). Three are unidentified sources (#32, #75 & 84), although two of these (#32 & 75) are in the vicinity of outer spiral arms in areas not covered by the optical survey of Matonick & Fesen (1997), and therefore stand as promising new candidate X-ray SNRs. Further optical/radio observations will be required to confirm their identifications.

The remaining three sources are consistent with the positions of known SNRs/HII radio sources. The *XMM* position of source #44 is consistent with that of SN1970G in the giant HII region NGC 5455, but in the absence of a more accurate *Chandra* position to confirm this association, it is possible that the X-ray emission we detect with *XMM* may be confused with other sources in the HII region where it resides. However, the *Chandra* position of source #67 shows that it is firmly associated with SNR MF65, with positions matching to within  $\sim 1$  arcsecond. In addition, the *Chandra* position of source #87 matches one of six radio sources detected by Eck et al. (2002) in the giant HII region NGC 5462. The authors do not classify this source as a SNR as it was only detected at 20 cm and hence has no measured spectral index. Even though we may just be detecting thermal X-ray emission from the HII region itself, this source does show a factor of  $\sim 7$  long-term decrease in X-ray luminosity between the *ROSAT* observations in 1992/1996, the *Chandra* observation in 2000 and the *XMM* observation in 2002, giving additional evidence that it may be a cooling SNR. Interestingly, this is one of the two sources that has a significant X-ray colour change between the *Chandra* and *XMM* observations, moving from the XRB to the SNR category with decreasing luminosity. This indicates that this source may be a recent supernova, with the colour change attributable to thermal source cooling.

In addition, there are two *XMM* sources that do not have SNR X-ray colours, but which do have SNR optical counterparts. Source #40 matches MF22 ( $\sim 1.7$  arcsecond offset), but falls into the XRB category. Although SNRs dominated by nonthermal emission (i.e. Crab-like SNR) will have harder X-ray spectra than thermal SNRs, we must bear in mind that XRBs and SNRs may in fact be spatially coincident, as both are the end products of massive stars and will tend to be located in star-forming regions. The other source (#46/XMM-1) demonstrates this point, as it is coincident with a SNR (MF37) although the spectral and timing properties of this source presented in Paper I show that it is an XRB.

### 7.4 Supersoft sources (SSSs)

SSSs have been detected in a number of galaxies (e.g. M31, Di Stefano et al. 2004; M81, Swartz et al. 2002; M83, Soria & Wu 2003) as well as M101 itself (Pence et al. 2001). They were classically defined as X-ray sources with effective temperatures of  $< 100$  eV, consistent with nuclear burning on the surface of white dwarfs accreting at high rates (Kahabka & van den Heuvel 1997; Greiner 2000). More recently, Di Stefano & Kong (2004) have extended this definition to include sources with either blackbody type spectra with  $kT < 175$  eV, or power-law spectra with  $\Gamma \geq 3.5$ , with less than 10 per cent of the total X-ray luminosity above 1.5 keV. This extended class is likely to represent a heterogeneous group including additional objects such as SNRs, accreting neutron stars or possibly even accreting intermediate-mass black holes (Di Stefano et al. 2004). For the majority of the sources in this *XMM* observation, we do not know the detailed spectral shapes of the sources, but we can identify candidate SSSs if emission is only detected in the softest (0.3–1 keV) energy band. The X-ray colour diagrams (Figure 3) show that 15 sources (marked with stars) fall into this category, with significant detections above  $3\sigma$  only in the soft band in either the PN and/or MOS data (#24, 31, 38, 43, 53, 56, 58, 62, 69, 71, 79, 80, 91, 95 & 100). Simulations in XSPEC show that a 175 eV blackbody EPIC (PN+MOS) spectrum would have approximate hardness ratio values of  $HR1=-0.66$  and  $HR2=-0.98$ , and the candidate SSSs hardness ratios are consistent with this, although as expected their hard  $HR2$  colours are mostly unconstrained. We can discount source #56 as a SSS candidate as it is positionally coincident with a foreground star (see section 7.5), but four sources (#53, 58, 71 & 100) are firmly associated with optically identified HII regions and the remainder generally lie on or near spiral arm structures as shown in the HI map in Figure 4 (top). No short-term variability is detected in any of these sources, but long-term variability is evident in sources #24, 43, 53, 58, 71, 91 & 100.

### 7.5 Foreground stars

Four *XMM* sources are positionally coincident with GSC stars (#3, 25, 56 & 105), and optical counterparts for an additional two (#21 & 78) have been identified as stars by Wang et al. (1999). Stars have soft thermal X-ray spectra, and the X-ray colours of sources #3, 21 & 56 are consistent with this, lying at the soft end of the absorbed, SNR and SSS categories respectively. In contrast, source #78 has a harder X-ray colour equivalent to  $\Gamma \sim 1.5$  and falls into the XRB category. Given that this source was only detected by the PSPC in the *ROSAT* observations and hence had large positional errors, it is feasible that it was mistakenly associated with a star-like optical counterpart by Wang et al. (1999). The *XMM* position of this source places it in an outer spiral arm of M101 near an HII region, and the X-ray properties make it more likely that this source is an XRB in M101 itself.

The remaining two sources are among the brightest X-ray sources in this field (#25=GSC1275 & #105=GSC1069[AG79] 10), and both have sufficient counts for spectral fitting. We have confirmed their identifications as stars (as opposed to background AGN) by fitting their *XMM* spectra in XSPEC v11.3 with a power-law model typically fit to AGN spectra, and MEKAL thermal plasma models which describe coronal emission from solar-type stars. The brightest source (#25) has a soft X-ray spectrum, with an X-ray flux of  $1.1 \times 10^{-13}$  erg cm $^{-2}$  s $^{-1}$ . It is poorly fit with a power-law model ( $\chi^2/dof=225/114$ ), and the slope of

$\Gamma=6.6$  is too steep for most AGN (typically  $\Gamma \sim 1.7 - 2.1$ , Nandra & Pounds 1994). It is, however, well fit with a two-temperature plasma ( $kT=0.37/1.01$  keV,  $\chi^2/dof=114/111$ ) with abundances of  $\sim 0.2Z_\odot$ , consistent with the temperatures and metallicities found in solar-type K-type stars (Briggs & Pye 2003). The light curve of this source also displays a classical flare with an exponential decay (see Figure 5, top), often seen in active K stars (Briggs & Pye 2003). The second source (#105) has an X-ray flux of  $4.3 \times 10^{-14}$  erg cm $^{-2}$  s $^{-1}$ , and is similarly well fit with a two-temperature plasma ( $kT=0.27/1.05$  keV,  $\chi^2/dof=36/38$ ) assuming abundances of  $\sim 0.3Z_\odot$  (leaving this parameter free resulted in unrealistically low values of  $\sim 0.1Z_\odot$ ). This time, the power-law fit is statistically acceptable ( $\chi^2/dof=46/39$ ), but the slope of  $\Gamma=4.9$  is again too steep for the vast majority of AGN. This source is also variable at  $> 3\sigma$  (see Figure 5, bottom).

## 8 SUMMARY

In this paper we have studied the properties of the X-ray point source population of M101 as seen with *XMM-Newton*. We detect 108 X-ray sources within the D<sub>25</sub> ellipse of M101, with fluxes ranging between  $3.1 \times 10^{-15} - 4.2 \times 10^{-13}$  erg cm $^{-2}$  s $^{-1}$  corresponding to luminosities of  $1.9 \times 10^{37} - 2.6 \times 10^{39}$  erg s $^{-1}$  in the 0.3–6 keV energy range at the distance of M101. We have studied the X-ray colour and variability characteristics of these sources, and have supplemented the *XMM* dataset with two archival *Chandra* observations in order to search for flux and spectral changes. The main results can be summarised as follows:

(i) Multiwavelength cross-correlations show that 20 sources are coincident with HII regions and/or SNRs, 7 have identified/candidate background AGN/galaxy counterparts, 6 are coincident with foreground stars and one has a radio counterpart. The remaining 74 are X-ray detections only.

(ii) The sources are distributed among the X-ray colour source categories as follows: 62 XRBs, 15 SNRs, 11 absorbed sources, 5 background sources and 15 candidate SSSs (those only detected significantly in the soft 0.3–1 keV band).

(iii) We estimate that  $\sim 24$  sources are background sources. Two sources are optically identified as background galaxies, one of which is the bright source XMM-5 from Paper I. A further five candidates background objects have been identified in the *ROSAT* study of M101 (Wang et al. 1999).

(iv) Approximately 60 per cent of the sources have X-ray colours consistent with XRBs. We estimate that half are associated with HII regions or spiral arm structure, with background AGN being the main contaminant in this category as they have similar spectral shapes.

(v) Fifteen sources have X-ray colours consistent with SNR. Two correlate with the positions of known SNRs, and another with a radio source in the giant HII region NGC 5462. Two sources are promising new candidate X-ray SNRs, one is unidentified, while the other nine are identified as stars, soft XRBs and AGN candidates.

(vi) Of the 15 sources with significant detections in the softest X-ray band (0.3–1 keV), 14 are candidate SSSs; four are firmly associated with HII regions and the remainder generally lie on or near spiral arm structure. The other source is coincident with a foreground star.

(vii) Four *XMM* sources are coincident with GSC stars, two of which are among the brightest X-ray sources in the field. Optical counterparts for an additional two sources have been identified as

stars by Wang et al. 1999, although one shows harder X-ray colours than expected for a star and may be an XRB located in a spiral arm.

(viii) Sixteen sources are found to be significantly ( $> 95$  per cent) variable during the *XMM-Newton* observation. Twelve of these fall into the XRB category, giving additional evidence that they are accreting systems. The remaining four fall into the SNR category; however these are all sources separately identified as either stars or soft XRBs.

(ix) Using archival *Chandra* and *ROSAT* data, we find that 44 ( $\sim 40$  per cent) *XMM* sources show long-term variability over a baseline of up to  $\sim 10$  years. One source is detected going through a transient phase in the *XMM* observation, while comparisons with archival data reveal seven sources exhibiting possible transient behaviour.

(x) Of the thirteen sources that vary significantly between the *Chandra* and *XMM* observations (excluding SSSs and foreground stars), only four show the canonical HS to LH state transition seen in Galactic black hole binary candidates, three of which are bright sources studied in Paper I. The remaining sources show the opposite behaviour, though this may simply be a consequence of the X-ray bands used to define the spectral changes.

We have shown that the X-ray colour scheme of Prestwich et al. (2003), adapted for the *XMM* EPIC instruments, can be a useful guide for source classification, and so can give valuable insights into the overall source population in a spiral galaxy. However, we also demonstrate that there are undoubtedly overlap regions in the colour-colour diagram due to the similar spectral shapes of sources of different natures. For example, soft XRBs may have colours equivalent to thermal SNRs, and background AGN can have colours in the same range as XRB systems.

This *XMM-Newton* observation has provided new information on the X-ray source population of M101, a spiral galaxy similar to the Milky Way. Using the spectral and timing properties of the brightest sources and the source classifications of the entire *XMM* catalogue, we have shown that this X-ray source population ( $L_X \sim 10^{37} - 10^{39}$  erg s $^{-1}$ ) is dominated by accreting sources (XRBs, SSSs). Further studies, such as the ongoing *Chandra* / *HST* 1 Ms deep observation program, will extend our knowledge to sources at lower luminosities and allow the identification of multiwavelength counterparts to confirm their identities. The useful methods developed in this study can now be extended to larger samples of local galaxies of different types, to detail and establish the properties of their X-ray source populations, search for statistical trends and characterize their overall X-ray emission properties. This in turn will provide us with the essential tools needed to interpret the X-ray emission detected from galaxies at higher redshifts.

## ACKNOWLEDGMENTS

This work is based on observations obtained with *XMM-Newton*, an ESA science mission with instruments and contributions directly funded by ESA and NASA. We thank the referee, Dr K. Mukai, for helpful comments on the original draft of this paper, and we thank K. Briggs for assistance with the source detection techniques. This research has made use of the SIMBAD database, operated at CDS, Strasbourg, France, and the NASA/IPAC Extragalactic Database (NED) which is operated by the Jet Propulsion Laboratory, California Institute of Technology, under contract with the National Aeronautics and Space Administration. The second digitized sky survey was produced by the Space Telescope Science Institute,

under Contract No. NAS 5-26555 with the National Aeronautics and Space Administration. The Guide Star Catalog was produced at the Space Telescope Science Institute under U.S. Government grant. These data are based on photographic data obtained using the Oschin Schmidt Telescope on Palomar Mountain and the UK Schmidt Telescope. LPJ is supported by a PPARC studentship.

## REFERENCES

Allen R. J., Goss W. M., 1979, *A&AS*, 36, 135  
 Braun R., 1995, *A&AS*, 114, 409  
 Bresolin F., Kennicutt R. C., Stetson P. B., 1996, *AJ*, 112, 1009  
 Briggs K. R., Pye J. P., 2003, *MNRAS*, 345, 714  
 Campana S., Moretti A., Lazzati D., Tagliaferri G., 2001, *ApJ*, 560, L19  
 Cedrés B., Cepa J., 2002, *A&A*, 391, 809  
 Chen C.-H. R., Chu Y., Gruendl R., Lai S., Wang Q. D., 2002, *AJ*, 123, 2462  
 Colbert E. J. M., Heckman T. M., Ptak A. F., Strickland D. K., Weaver K. A., 2004, *ApJ*, 602, 231  
 de Vaucouleurs G., de Vaucouleurs A., Corwin H. G., Buta R. J., Paturel G., Fouque P., 1991, *trcb.book*,  
 Dewangan G. C., Miyaji T., Griffiths R. E., Lehmann I., 2004, *ApJ*, 608, L57  
 Dickey J. M., Lockman F. J., 1990, *ARA&A*, 28, 215  
 Di Stefano R., Kong A. K. H., 2004, preprint (astro-ph/0311374)  
 Di Stefano R., et al., 2004a, *ApJ*, 610, 247  
 Di Stefano R., Primini F. A., Kong A. K. H., Russo T., 2004b, preprint (astro-ph/0405238)  
 Eck C. R., Cowan J. J., Branch D., 2002, *ApJ*, 573, 306  
 Fabbiano G., Trinchieri G., 1987, *ApJ*, 315, 46  
 Fabbiano G., 1989, *ARA&A*, 27, 87  
 Fabbiano G., Zezas A., King A. R., Ponman T. J., Rots A., Schweizer F., 2003, *ApJ*, 584, L5  
 Greiner J., 2000, *NewA*, 5, 137  
 Hodge P. W., 1969, *ApJS*, 18, 73  
 Hodge P. W., Kennicutt R. C., 1983, *AJ*, 88, 296  
 Hodge P. W., Gurwell M., Goldader J. D., Kennicutt R. C., 1990, *ApJS*, 73, 661  
 Israel F. P., Goss W. M., Allen R. J., 1975, *A&A*, 40, 421  
 Jenkins L. P., Roberts T. P., Warwick R. S., Kilgard R. E., Ward M. J., 2004, *MNRAS*, 349, 404  
 Kahabka P., van den Heuvel E. P. J., 1997, *ARA&A*, 35, 69  
 Kamphuis J., Sancisi R., van der Hulst T., 1991, *A&A*, 244, L29  
 Kilgard R. E., Kaaret P., Krauss M. I., Prestwich A. H., Raley M. T., Zezas A., 2002, *ApJ*, 573, 138  
 Kilgard R. E., Cowan J. J., Garcia M. R., et al., 2004, submitted to *ApJS*  
 King A. R., 2002, *MNRAS*, 335, L13  
 King A. R., 2004, van der Klis M., eds, *Compact Stellar X-Ray Sources*, Cambridge Univ. Press, Cambridge, in press (astro-ph/0301118)  
 Kuntz K. D., Snowden S. L., Pence W. D., Mukai K., 2003, *ApJ*, 588, 264  
 Lai S., Chu Y., Chen C.-H. R., Ciardullo R., Grebel E. K., 2001, *ApJ*, 547, 754  
 Matonick D. M., Fesen R. A., 1997, *ApJS*, 112, 49  
 McCammon D., Sanders W. T., 1984, *ApJ*, 287, 167  
 McClintock J. E., Remillard R. A., 2004, van der Klis M., eds, *Compact Stellar X-Ray Sources*, Cambridge Univ. Press, Cambridge, in press (astro-ph/0306213)  
 Menou K., Esin A. A., Narayan R., Garcia M. R., Lasota J., McClintock J. E., 1999, *ApJ*, 520, 276  
 Miller, M. C., Colbert E. J. M., 2004, *Int. J. Mod. Phys. D*, 13, 1  
 Mukai K., Pence W. D., Snowden S. L., Kuntz K. D., 2003, *ApJ*, 582, 184  
 Nandra K., Pounds K. A., 1994, *MNRAS*, 268, 405  
 Page M. J., Mittaz J. P. D., Carrera F. J., 2001, *MNRAS*, 325, 575  
 Pence W. D., Snowden S. L., Mukai K., Kuntz K. D., 2001, *ApJ*, 561, 189  
 Pietsch W., Roberts T. P., Sako M., et al., 2001, *A&A*, 365, L174  
 Pietsch W., Misanovic Z., Haberl F., Hatzidimitriou D., Ehle M., Trinchieri G., 2004, *A&A*, 426, 11  
 Prestwich A. H., Irwin J. A., Kilgard R. E., Krauss M. I., Zezas A., Primini F., Kaaret P., Boroson B., 2003, *ApJ*, 595, 719  
 Read A. M., Ponman T. J., Strickland D. K., 1997, *MNRAS*, 286, 626  
 Roberts T. P., Warwick R. S., 2000, *MNRAS*, 315, 98  
 Roberts T. P., Warwick R. S., Ward M. J., Goad M. R., 2004, *MNRAS*, 349, 1193  
 Sanduleak N., Pesch P., 1987, *ApJS*, 63, 809  
 Searle L., 1971, *ApJ*, 168, 327  
 Snowden S. L., Pietsch W., 1995, *ApJ*, 452, 627  
 Snowden S. L., Mukai K., Pence W., Kuntz K. D., 2001, *AJ*, 121, 3001  
 Soria R., Wu K., 2003, *A&A*, 410, 53  
 Stetson P. B., Saha A., Ferrarese L., et al., 1998, *ApJ*, 508, 491  
 Swartz D. A., Ghosh K. K., Suleimanov V., Tennant A. F., Wu K., 2002, *ApJ*, 574, 382  
 Trinchieri G., Fabbiano G., Romaine S., 1990, *ApJ*, 356, 110  
 Wang Q. D., Immel S., Pietsch W., 1999, *ApJ*, 523, 121  
 Williams R. M., Chu Y., 1995, *ApJ*, 439, 132